Available online at www.sciencedirect.com
SCIENCE DIRECT®
ELSEVIER
International Journal of Solids and Structures 43 (2006) 4830–4866
INTERNATIONAL JOURNAL OF SOLIDS and STRUCTURES
www.elsevier.com/locate/ijsolstr

Dynamic stress intensity factors for homogeneous and smoothly heterogeneous materials using the interaction integral method

Seong Hyeok Song, Glaucio H. Paulino *

Department of Civil and Environmental Engineering, University of Illinois at Urbana-Champaign, Newmark Laboratory, 205 North Mathews Avenue, Urbana, IL 61801, USA

Received 7 April 2005; received in revised form 17 June 2005
Available online 10 October 2005

Abstract

Dynamic stress intensity factors (DSIFs) are important fracture parameters in understanding and predicting dynamic fracture behavior of a cracked body. To evaluate DSIFs for both homogeneous and non-homogeneous materials, the interaction integral (conservation integral) originally proposed to evaluate SIFs for a static homogeneous medium is extended to incorporate dynamic effects and material non-homogeneity, and is implemented in conjunction with the finite element method (FEM). The technique is implemented and verified using benchmark problems. Then, various homogeneous and non-homogeneous cracked bodies under dynamic loading are employed to investigate dynamic fracture behavior such as the variation of DSIFs for different material property profiles, the relation between initiation time and the domain size (for integral evaluation), and the contribution of each distinct term in the interaction integral.

Keywords: Dynamic stress intensity factors (DSIFs); Interaction integral; Non-homogeneous materials; Functionally graded materials (FGMs)

1. Introduction

Static and dynamic fracture behavior of homogeneous and non-homogeneous cracked bodies can be understood and predicted, to a certain extent, once stress intensity factors (SIFs) are known. Thus, an

* Corresponding author. Tel.: +1 217 333 3817; fax: +1 217 265 8041.
E-mail addresses: shsong@uiuc.edu (S.H. Song), paulino@uiuc.edu (G.H. Paulino).

0020-7683/$ - see front matter © 2005 Elsevier Ltd. All rights reserved.
doi:10.1016/j.ijsolstr.2005.06.102

accurate evaluation of SIFs is crucial in fracture mechanics for both static and dynamic cases as they can be used to investigate crack initiation and propagation. Several methods have been developed and applied by many researchers to evaluate DSIFs for various problems, as discussed below.

For homogeneous materials, Chen (1975) examined a centrally cracked rectangular finite strip subjected to step loading using a Lagrangian finite difference method (FDM). DSIFs were obtained from the relation between DSIFs and stress fields in the vicinity of a crack tip. This problem has been considered as a benchmark problem and explored by many researchers. Aoki et al. (1978) utilized the relationship between displacements and DSIFs to obtain mode I or mode III DSIFs. Kishimoto et al. (1980) proposed a modified path-independent J-integral, which involves the inertial effects to determine DSIFs in conjunction with the finite element method (FEM), and employed a decomposition procedure for mixed-mode problems. Brickstad (1983) used an explicit time scheme in a special FEM program to evaluate DSIFs. By means of the relationship between SIFs and crack opening displacement, DSIFs were determined without singular elements. Murti and Valliappan (1986) examined various problems, such as Chen's problem (1975), using quarter-point elements (QPEs) and the FEM. DSIFs were evaluated from the relation between the first two coefficients of Williams (1957) solution and the finite element displacement in the vicinity of the crack. The effect of QPE size was assessed qualitatively in their works. Lee and Freund (1990) solved mixed mode problems of a semi-infinite plate containing an edge crack under an impact loading and determined DSIFs through linear superposition of several stress wave propagation solutions. Lin and Ballmann (1993) revisited Chen's problem (1975) using the Lagrangian FDM. They adopted the same technique by Chen (1975) to evaluate DSIFs. Their numerical results are almost identical with those obtained by Chen except for a few time periods when wave fluctuations occurs. They contended that Chen (1975) used too few cells to capture actual peaks of DSIFs. Dominguez and Gallego (1992) computed DSIFs using time domain boundary element method with singular quarter-point boundary elements. Fedelinski et al. (1994) adopted the $\widehat{J}$-integral to obtain DSIFs by means of the dual boundary element method. In the $\widehat{J}$-integral approach, the mode decomposition procedure is employed for mixed mode problems. Belytschko (1995) determined static and dynamic SIFs using the Element Free Galerkin (EFG) method, which is a meshless method based on moving least square interpolants. The DSIFs were calculated by conservation integrals, which directly evaluate the individual SIFs for the mixed mode problem in terms of known auxiliary solutions. Sladek et al. (1997, 1999) used the $\widehat{J}$-integral to determine DSIFs in conjunction with the boundary element method (BEM). They proposed the interaction integral for the computation of T-stress (non-singular stress), and the $\widehat{J}$-integral for the evaluation of DSIFs. Krysl and Belytschko (1999) investigated three-dimensional (3D) stationary and dynamically propagating crack problems. DSIFs were obtained from the interaction integral in conjunction with the EFG method. Zhang (2002) explored transient dynamic problems using hypersingular time-domain traction BEM. DSIFs were obtained from relating the crack tip opening displacements and SIFs. Tabiei and Wu (2003) investigated fracture behavior including DSIFs and energy release rate for a cracked body subjected to dynamic loadings using DYNA3D (Whirley and Engelmann, 1993), which is a non-linear explicit finite element code. An element deletion-and-replacement remeshing scheme was employed using the FEM to simulate crack propagation. Enderlein et al. (2003) investigated fracture behavior for two-dimensional (2D) and 3D cracked bodies under impact loading using FEM. They adopted the J-integral, the modified crack closure integral and the displacement correlation technique to evaluate pure mode I DSIFs. Fedelinski (2004) applied the dual BEM in conjunction with the time domain, the integral transform and the dual reciprocity methods for dynamic analysis of cracked media where DSIFs were computed using the relationship between path independent integral and crack opening displacements.

For non-homogeneous materials, Rousseau and Tippur (2001) obtained DSIFs for FGMs both numerically and experimentally. The DSIFs prior to crack initiation were determined utilizing asymptotic fields of Williams' solution (1957), which is equivalent to the stationary fields. After initiation, the crack tip fields for steadily growing cracks in FGMs, obtained by Parameswaran and Shukla (1999), were used to obtain

DSIFs. Material gradients were employed in the commercial software ABAQUS (2004) by applying temperature, which is a function of material properties, and by letting the coefficient of thermal expansion be zero. As the distance is close to the crack tip, the DSIFs were underestimated because no singular elements were used. Therefore, regression technique was employed to obtain DSIFs at the crack tip based on the displacement correlation technique (DCT). Wu et al. (2002) extended the J-integral to incorporate material gradients and dynamic effects. They evaluated J for a single edge cracked FGM panel under step loading in conjunction with the EFG method. Santare et al. (2003) investigated elastic wave propagation for uncracked non-homogeneous media.

Although a few researchers (Rousseau and Tippur, 2001; Wu et al., 2002) evaluated fracture quantities such as SIFs or J for non-homogeneous cracked bodies under dynamic loading, only mode I SIF, i.e., K_I, is evaluated in conjunction with either the J-integral or the DCT. Furthermore, several important fracture behavior of non-homogeneous cracked bodies have not been investigated thoroughly. So, the scope of this study follows:

- The interaction integral (M-integral), which is known to be superior to the DCT and J-integral, is extended to incorporate material non-homogeneity and dynamic effects for evaluation of DSIFs.
- Various mixed-mode problems under dynamic loadings are adopted to compute dynamic K_I and K_{II}.
- Several important fracture behavior of non-homogeneous cracked bodies under dynamic loadings such as the variation of mixed-mode DSIFs for different material property profiles are explored in detail.

This paper is organized as follows. Section 2 addresses numerical schemes for incorporating material non-homogeneity and dynamic finite element formulation. Section 3 describes dynamic auxiliary fields for non-homogeneous materials. Section 4 presents various theoretical and numerical aspects of the interaction integral and M-integral. Section 5 provides the verification of the research code developed to evaluate SIFs and DSIFs for both homogenous and non-homogeneous materials employing benchmark problems. Section 6 shows and discusses dynamic fracture behavior such as variation of DISFs for various homogeneous and non-homogeneous cracked bodies under dynamic loading. Finally, conclusions are presented.

2. Numerical scheme

In this section, the concept of isoparametric finite element formulation for incorporating non-homogeneous material properties at the element level is addressed and the average acceleration method is presented briefly.

2.1. Generalized Isoparametric Formulation (GIF)

To incorporate material non-homogeneity, we can use either graded elements or homogeneous elements. Graded elements incorporate the material property gradient at the size scale of the element, while the homogeneous element produces a stepwise constant approximation to a continuous material property field. In general, graded elements approximate the actual material gradations better than homogeneous elements. The difference of numerical results using two different schemes can be more distinct for relatively coarse meshes where the material gradation is steep. Kim and Paulino (2002a) investigated the performance of both elements for non-homogeneous materials where material gradations are either parallel or perpendicular to the applied external loading such as bending, tension and fixed grip loading. Buttlar et al. (2005) applied both schemes in pavement systems where material gradations occur due to temperature gradients

and aging related stiffness gradients using the UMAT capability of the finite element software ABAQUS (2004). The authors of both works concluded that graded elements lead to more accurate unaveraged stress along the interface where material properties are not continuous.

The *Generalized Isoparametric Formulation* (GIF) of Kim and Paulino (2002a) consists of interpolating geometry, displacements and material properties from nodal points. Thus, material properties such as elastic modulus (E), Poisson's ratio (v), and mass density (ρ) at Gauss points can be interpolated using shape functions from nodal points as follows:

$$E = \sum_i N_i(\xi,\eta)E_i, \quad v = \sum_i N_i(\xi,\eta)v_i, \quad \rho = \sum_i N_i(\xi,\eta)\rho_i, \tag{1}$$

where N_i are the shape functions, which are functions of the intrinsic coordinates ξ and η. This formulation is implemented in the present code.

2.2. Average acceleration method

Newmark (1959) proposed a family of direct integration schemes, which has been widely used in dynamic analysis. An acceleration form of the Newmark method with the zero viscous damping matrix, i.e.,$\boldsymbol{C} = \boldsymbol{0}$, is given as (Hughes, 1987)

$$(\boldsymbol{M} + \beta\Delta t^2\boldsymbol{K})\ddot{\boldsymbol{d}}_n = \boldsymbol{r}_n^{\text{ext}} - \boldsymbol{K}\left(\boldsymbol{d}_{n-1} + \Delta t\dot{\boldsymbol{d}}_{n-1} + \frac{\Delta t^2}{2}(1-2\beta)\ddot{\boldsymbol{d}}_{n-1}\right), \tag{2}$$

in which Δt denotes the time step, $\boldsymbol{r}^{\text{ext}}$ is the vector of applied forces, $(n-1)$ and (n) indicate the previous step and the current step, respectively, $\boldsymbol{d}$, $\dot{\boldsymbol{d}}$ and $\ddot{\boldsymbol{d}}$ represent the displacement, velocity and acceleration vectors, respectively, and $\boldsymbol{M}$ and $\boldsymbol{K}$ stand for the mass matrix, and the stiffness matrix, respectively. Once $\ddot{\boldsymbol{d}}_n$ is determined through Eq. (2), $\boldsymbol{d}_n$ and $\dot{\boldsymbol{d}}_n$ can be evaluated as follows:

$$\boldsymbol{d}_n = \boldsymbol{d}_{n-1} + \Delta t\dot{\boldsymbol{d}}_{n-1} + \frac{\Delta t^2}{2}(1-2\beta)\ddot{\boldsymbol{d}}_{n-1} + \beta\Delta t^2\ddot{\boldsymbol{d}}_n, \tag{3}$$

$$\dot{\boldsymbol{d}}_n = \dot{\boldsymbol{d}}_{n-1} + (1-\gamma)\Delta t\ddot{\boldsymbol{d}}_{n-1} + \gamma\Delta t\ddot{\boldsymbol{d}}_n, \tag{4}$$

respectively. In this formulation, when $\gamma = 1/2$ and $\beta = 1/4$, the method is called an average acceleration method, which is implicit and unconditionally stable with second order accuracy.

3. On dynamic auxiliary fields for non-homogeneous materials

The interaction integral utilizes two admissible fields: auxiliary and actual fields. Auxiliary fields are based on known fields such as Williams' solution (1957), while actual fields utilize quantities such as displacements, strains and stresses obtained by means of numerical methods, e.g., FEM. In this section, the choice of the auxiliary fields is discussed thoroughly. Then, a non-equilibrium formulation, consisting of terms owing to material non-homogeneity, is presented in conjunction with the auxiliary fields.

3.1. Choice of auxiliary fields

An appropriate choice of auxiliary fields leads to the computation of SIFs by means of the interaction integral or M-integral. The auxiliary fields should be suitably defined and contain the quantities to be determined, i.e., K_{I} and K_{II}. Yau et al. (1980) adopted Williams' solution (1957) as the auxiliary fields to evaluate SIFs for a homogeneous cracked body. Dolbow and Gosz (2000), Rao and Rahman (2003), and Kim and

Paulino (2003a) employed this same auxiliary fields for a non-homogeneous cracked body under quasi-static conditions. Sladek et al. (1999) defined the elastostatic field, i.e., $\sigma^{\text{aux}}_{ij,j} = 0$, as dynamic auxiliary field for the computation of T-stress of a homogeneous medium. In the present work, the asymptotic fields of Williams' solution (1957) are employed as the auxiliary fields for dynamic non-homogeneous materials, because the dynamic asymptotic fields of non-homogeneous materials show similar behavior to those of quasi-static homogeneous materials around the crack tip locations (Eischen, 1987; Freund, 1998; Freund and Clifton, 1974; Nilsson, 1974; Parameswaran and Shukla, 1999).

The asymptotic auxiliary stress fields, defined according to the illustration in Fig. 1, are given by (Eftis et al., 1977)

$$\sigma^{\text{aux}}_{ij} = K^{\text{aux}}_{\text{I}} f^{\text{I}}_{ij}(r,\theta) + K^{\text{aux}}_{\text{II}} f^{\text{II}}_{ij}(r,\theta) \quad (i,j=1,2) \tag{5}$$

and the corresponding auxiliary displacement fields are

$$u^{\text{aux}}_{i} = \frac{K^{\text{aux}}_{\text{I}}}{\mu_{\text{tip}}} g^{\text{I}}_{i}(r,\theta) + \frac{K^{\text{aux}}_{\text{II}}}{\mu_{\text{tip}}} g^{\text{II}}_{i}(r,\theta) \quad (i=1,2), \tag{6}$$

where μ_{tip} is the shear modulus at the crack tip, and $K^{\text{aux}}_{\text{I}}$ and $K^{\text{aux}}_{\text{II}}$ are the auxiliary mode I and mode II SIFs, respectively. The standard functions $f_{ij}(r,\theta)$ and $g_i(r,\theta)$ are provided in several texts, e.g., Anderson's book (1995).

As mentioned earlier, the asymptotic fields of Williams' solution (1957) are selected as the auxiliary fields to evaluate DSIFs in conjunction with the M-integral in this work. When a finite domain is chosen to evaluate the M-integral, however, these auxiliary fields cannot hold except for the crack tip location due to non-homogeneous material properties. This aspect is noticeable when auxiliary fields are evaluated at finite distances from the crack tip. As a consequence, extra terms appear in the formulation to compensate for the difference in response due to material non-homogeneity.

3.2. Formulations

Due to the difference between material properties at the crack tip and away from the tip, three different formulations, which are non-equilibrium, incompatibility and constant constitutive tensor, were derived. The additional terms and the corresponding formulations for non-homogeneous materials have been discussed by various researchers. Dolbow and Gosz (2000) proposed the incompatibility formulation and used this formulation to obtain SIFs for an arbitrarily oriented crack in FGMs using the extended

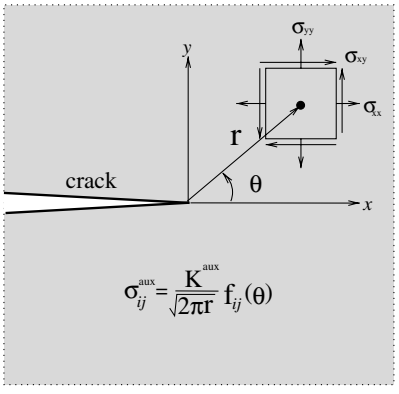

Fig. 1. Williams' (1957) solution for SIF evaluation. Here x and y indicate the local coordinate system.

FEM. They also discussed non-equilibrium and constitutive tensor formulations. Rao and Rahman (2003) employed the constant constitutive tensor and the incompatibility formulations to evaluate SIFs for FGMs by means of the Element Free Galerkin (EFG) method. Kim and Paulino (2003a) proposed the non-equilibrium formulation to determine SIFs for various cracked FGMs in conjunction with FEM. Theoretically, this non-equilibrium formulation is equivalent to the incompatibility formulation and the constant constitutive tensor formulation. From a numerical point of view, however, the accuracy of the constant constitutive tensor formulation might not be as good as the other two formulations because it incorporates derivatives of the actual stress and strain fields, which are evaluated numerically (Song, 2003). In this work, the non-equilibrium term and the corresponding non-equilibrium formulation are used in conjunction with FEM to determine DSIFs for arbitrarily oriented cracks in non-homogeneous materials under dynamic loading.

3.3. Non-equilibrium formulation

The field quantities from Williams' solution such as displacements, strains and stresses should be evaluated properly in order to be valid as the auxiliary fields. But all quantities cannot be used at the same time because they are valid at the crack tip location and not valid at other points due to non-homogeneity. Therefore, only two quantities can be selected from Williams' solution and the other quantity is obtained by considering material non-homogeneity.

In this formulation, the auxiliary displacements and strains are obtained directly from Williams' solution and the auxiliary stresses are evaluated from the non-homogeneous constitutive model. The auxiliary displacement is given by Eq. (6). Then auxiliary strain fields are obtained using the relation between strain and displacement

$$\varepsilon_{ij}^{\text{aux}} = \frac{1}{2}(u_{i,j}^{\text{aux}} + u_{j,i}^{\text{aux}}). \tag{7}$$

Finally, the auxiliary stress is obtained from

$$\sigma_{ij}^{\text{aux}} = C_{ijkl}(\boldsymbol{x})\varepsilon_{kl}^{\text{aux}}, \tag{8}$$

where $C_{ijkl}(\boldsymbol{x})$ is a constitutive tensor which varies spatially.

Since displacement and strains are obtained from the Williams' solutions directly, the compatibility condition is satisfied. However, the auxiliary stress field does not satisfy the equilibrium equation, i.e., $\sigma_{ij,j}^{\text{aux}} \neq 0$, because the constitutive tensor consists of material properties, which are functions of location. This condition will lead to a non-equilibrium term in the formulation.

4. Theoretical and numerical aspects of the interaction integral

In this section, the interaction integral is formulated by superimposing the actual and auxiliary fields on the path independent J-integral (Rice, 1968). Based on the interaction integral, the derivation of non-equilibrium based M-integral is performed. Various numerical aspects of the M-integral are presented. Computation of SIFs is explained in conjunction with the M-integral.

4.1. Interaction integral formulation

Assuming that the crack faces are traction-free and using the weight function q varying from unity at the crack tip to zero on Γ_0 according to Fig. 2, the generalized J-integral becomes

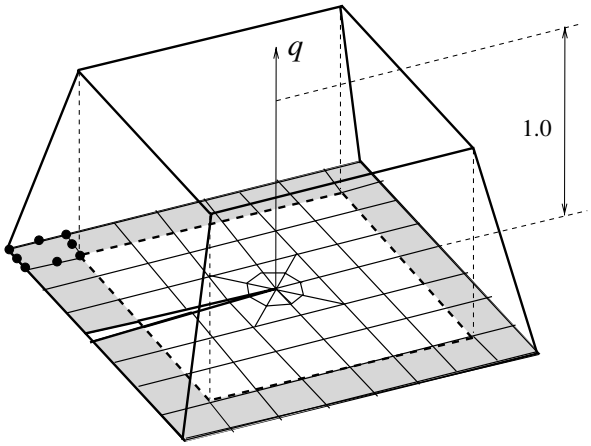

Fig. 2. The q function (plateau weight function).

$$J = \lim_{\Gamma_s \to 0} \int_{\Gamma_s} (W\delta_{1j} - \sigma_{ij}u_{i,1})n_j \, d\Gamma = -\lim_{\Gamma_s \to 0} \oint_{\Gamma} (W\delta_{1j} - \sigma_{ij}u_{i,1})m_j q \, d\Gamma, \tag{9}$$

where W is the strain energy density, $\Gamma = \Gamma_0 + \Gamma^+ - \Gamma_s + \Gamma^-$, and m_j is a unit normal vector to the contour (Γ), as illustrated in Fig. 3.

Application of the divergence theorem to Eq. (9) leads to the equivalent domain integral (EDI) (Raju and Shivakumar, 1990) as follows:

$$J = \int_A (\sigma_{ij}u_{i,1} - W\delta_{1j})q_{,j} \, dA + \int_A (\sigma_{ij}u_{i,1} - W\delta_{1j})_{,j} q \, dA. \tag{10}$$

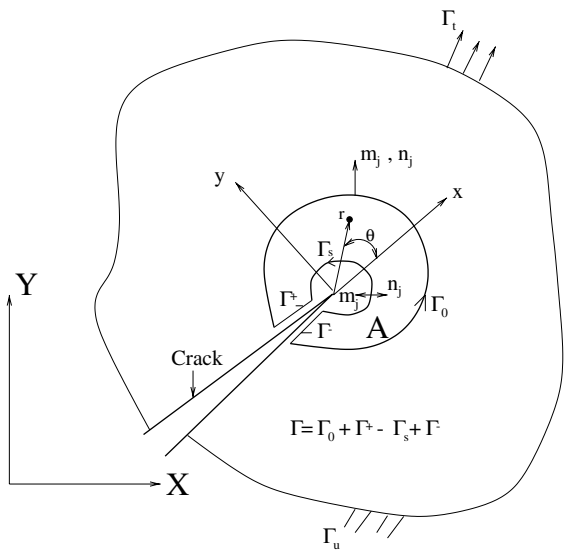

Fig. 3. Transformation from line integral to equivalent domain integral (EDI) (Raju and Shivakumar, 1990). Notice that the normal vector $m_j = n_j$ for Γ_0, Γ^+ and Γ^-, and $m_j = -n_j$ on Γ_s.

Considering the following relationships, which can be applied for general cases including material gradient and dynamic effects,

$$W_{,1} = \frac{1}{2}\sigma_{ij,1}\varepsilon_{ij} + \frac{1}{2}\sigma_{ij}\varepsilon_{ij,1} \tag{11}$$

and

$$(\sigma_{ij}u_{i,1})_{,j} = \sigma_{ij,j}u_{i,1} + \sigma_{ij}u_{i,1j}, \tag{12}$$

one obtains the following expression:

$$J = \int_A (\sigma_{ij}u_{i,1} - W\delta_{1j})q_{,j}\,\mathrm{d}A + \int_A \left(\sigma_{ij,j}u_{i,1} + \sigma_{ij}u_{i,1j} - \frac{1}{2}\sigma_{ij,1}\varepsilon_{ij} - \frac{1}{2}\sigma_{ij}\varepsilon_{ij,1}\right)q\,\mathrm{d}A, \tag{13}$$

which is modified as

$$J = \int_A (\sigma_{ij}u_{i,1} - W\delta_{1j})q_{,j}\,\mathrm{d}A + \int_A \left(\rho\ddot{u}_i u_{i,1} - \frac{1}{2}C_{ijkl,1}\varepsilon_{ij}\varepsilon_{kl}\right)q\,\mathrm{d}A, \tag{14}$$

using the following equalities:

$$\begin{aligned}
&\sigma_{ij,j} = \rho\ddot{u}_i,\\
&\sigma_{ij,1}\varepsilon_{ij} = (C_{ijkl}\varepsilon_{kl})_{,1}\varepsilon_{ij} = \left(C_{ijkl,1}\varepsilon_{kl}\varepsilon_{ij} + \sigma_{ij}\varepsilon_{ij,1}\right),\\
&\sigma_{ij}u_{i,1j} = \sigma_{ij}\varepsilon_{ij,1},
\end{aligned} \tag{15}$$

where C_{ijkl} denotes the elasticity tensor. Notice that Eq. (14) is the extended *J-integral under the stationary condition*. Eq. (14) is reduced to the *J*-integral for the static non-homogeneous material case as derived by Kim and Paulino (2002b). Besides, for homogeneous materials, Eq. (14) is identical to the one derived by Moran and Shih (1987) under the stationary condition, i.e., $V = 0$.

Superimposing the actual and auxiliar fields on Eq. (13), one obtains

$$\begin{aligned}
J = &\int_A \left\{(\sigma_{ij}^{\mathrm{aux}} + \sigma_{ij})(u_{i,1}^{\mathrm{aux}} + u_{i,1}) - \frac{1}{2}(\sigma_{ik}^{\mathrm{aux}} + \sigma_{ik})(\varepsilon_{ik}^{\mathrm{aux}} + \varepsilon_{ik})\delta_{1j}\right\}q_{,j}\,\mathrm{d}A\\
&+ \int_A \left\{(\sigma_{ij,j}^{\mathrm{aux}} + \sigma_{ij,j})(u_{i,1}^{\mathrm{aux}} + u_{i,1}) + (\sigma_{ij}^{\mathrm{aux}} + \sigma_{ij})(u_{i,1j}^{\mathrm{aux}} + u_{i,1j})\right\}q\,\mathrm{d}A\\
&- \frac{1}{2}\int_A \left\{(\sigma_{ij,1}^{\mathrm{aux}} + \sigma_{ij,1})(\varepsilon_{ij}^{\mathrm{aux}} + \varepsilon_{ij}) + (\sigma_{ij}^{\mathrm{aux}} + \sigma_{ij})(\varepsilon_{ij,1}^{\mathrm{aux}} + \varepsilon_{ij,1})\right\}q\,\mathrm{d}A,
\end{aligned} \tag{16}$$

which is decomposed into

$$J^s = J + J^{\mathrm{aux}} + M, \tag{17}$$

where J and J^{aux} are given by

$$\begin{aligned}
J = &\int_A \left(\sigma_{ij}u_{i,1} - \frac{1}{2}\sigma_{ik}\varepsilon_{ik}\delta_{1j}\right)q_{,j}\,\mathrm{d}A\\
&\int_A \left(\sigma_{ij,j}u_{i,1} + \sigma_{ij}u_{i,1j} - \frac{1}{2}\sigma_{ij,1}\varepsilon_{ij} - \frac{1}{2}\sigma_{ij}\varepsilon_{ij,1}\right)q\,\mathrm{d}A,
\end{aligned} \tag{18}$$

$$J^{\text{aux}} = \int_A \left(\sigma_{ij}^{\text{aux}} u_{i,1}^{\text{aux}} - \frac{1}{2} \sigma_{ik}^{\text{aux}} \varepsilon_{ik}^{\text{aux}} \delta_{1j} \right) q_{,j} \, \mathrm{d}A$$
$$\int_A \left(\sigma_{ij,j}^{\text{aux}} u_{i,1}^{\text{aux}} + \sigma_{ij}^{\text{aux}} u_{i,1j}^{\text{aux}} - \frac{1}{2} \sigma_{ij,1}^{\text{aux}} \varepsilon_{ij}^{\text{aux}} - \frac{1}{2} \sigma_{ij}^{\text{aux}} \varepsilon_{ij,1}^{\text{aux}} \right) q \, \mathrm{d}A, \tag{19}$$

respectively. The resulting M-integral is given by

$$M = \int_A \left\{ (\sigma_{ij}^{\text{aux}} u_{i,1} + \sigma_{ij} u_{i,1}^{\text{aux}}) - \frac{1}{2} (\sigma_{ik}^{\text{aux}} \varepsilon_{ik} + \sigma_{ik} \varepsilon_{ik}^{\text{aux}}) \delta_{1j} \right\} q_{,j} \, \mathrm{d}A$$
$$+ \int_A \left\{ (\sigma_{ij,j}^{\text{aux}} u_{i,1} + \sigma_{ij,j} u_{i,1}^{\text{aux}}) + (\sigma_{ij}^{\text{aux}} u_{i,1j} + \sigma_{ij} u_{i,1j}^{\text{aux}}) \right\} q \, \mathrm{d}A$$
$$- \frac{1}{2} \int_A \left\{ (\sigma_{ij,1}^{\text{aux}} \varepsilon_{ij} + \sigma_{ij,1} \varepsilon_{ij}^{\text{aux}}) + (\sigma_{ij}^{\text{aux}} \varepsilon_{ij,1} + \sigma_{ij} \varepsilon_{ij,1}^{\text{aux}}) \right\} q \, \mathrm{d}A. \tag{20}$$

4.2. Non-equilibrium formulation

This formulation creates the non-equilibrium terms explained in Section 3.3. Since the actual fields employ the quantities obtained from numerical simulation, the equilibrium and compatibility condition are satisfied, i.e.,

$$\sigma_{ij,j} = \rho \ddot{u}_i, \tag{21}$$

$$\varepsilon_{ij} = \frac{1}{2} (u_{i,j} + u_{j,i}), \quad \sigma_{ij} u_{i,1j} = \sigma_{ij} \varepsilon_{ij,1}. \tag{22}$$

For the auxiliary fields, the equilibrium condition is not satisfied, i.e.,

$$\sigma_{ij,j}^{\text{aux}} \neq 0, \tag{23}$$

while the relation between strain and displacement are compatible

$$\varepsilon_{ij}^{\text{aux}} = \frac{1}{2} (u_{i,j}^{\text{aux}} + u_{j,i}^{\text{aux}}), \quad \sigma_{ij} u_{i,1j}^{\text{aux}} = \sigma_{ij} \varepsilon_{ij,1}^{\text{aux}}. \tag{24}$$

Notice that the auxiliary fields are chosen as asymptotic fields for static homogeneous materials as explained in Section 3.1. For the superimposed actual and auxiliary fields, the following equalities are obtained:

$$\sigma_{ij} \varepsilon_{ij}^{\text{aux}} = C_{ijkl}(\boldsymbol{x}) \varepsilon_{kl} \varepsilon_{ij}^{\text{aux}} = \sigma_{kl}^{\text{aux}} \varepsilon_{kl} = \sigma_{ij}^{\text{aux}} \varepsilon_{ij}, \tag{25}$$

$$C_{ijkl,1}(\boldsymbol{x}) \varepsilon_{kl}^{\text{aux}} \varepsilon_{ij} = C_{ijkl,1}(\boldsymbol{x}) \varepsilon_{ij}^{\text{aux}} \varepsilon_{kl}, \tag{26}$$

$$C_{ijkl}(\boldsymbol{x}) \varepsilon_{kl,1} \varepsilon_{ij}^{\text{aux}} = \sigma_{ij}^{\text{aux}} \varepsilon_{ij,1}, \tag{27}$$

$$C_{ijkl}(\boldsymbol{x}) \varepsilon_{kl,1}^{\text{aux}} \varepsilon_{ij} = \sigma_{ij} \varepsilon_{ij,1}^{\text{aux}}. \tag{28}$$

Substitution of Eqs. (21) and (25) into Eq. (20) leads to

$$M = \int_A \left\{ (\sigma_{ij}^{\text{aux}} u_{i,1} + \sigma_{ij} u_{i,1}^{\text{aux}}) - \sigma_{ik}^{\text{aux}} \varepsilon_{ik} \delta_{1j} \right\} q_{,j} \, \mathrm{d}A$$
$$+ \int_A \left\{ \sigma_{ij,j}^{\text{aux}} u_{i,1} + \rho \ddot{u}_i u_{i,1}^{\text{aux}} + (\sigma_{ij}^{\text{aux}} u_{i,1j} + \sigma_{ij} u_{i,1j}^{\text{aux}}) \right\} q \, \mathrm{d}A$$
$$- \frac{1}{2} \int_A \left\{ (\sigma_{ij,1}^{\text{aux}} \varepsilon_{ij} + \sigma_{ij,1} \varepsilon_{ij}^{\text{aux}}) + (\sigma_{ij}^{\text{aux}} \varepsilon_{ij,1} + \sigma_{ij} \varepsilon_{ij,1}^{\text{aux}}) \right\} q \, \mathrm{d}A. \tag{29}$$

Since $\sigma_{ij}^{\text{aux}} = C_{ijkl}(\boldsymbol{x})\varepsilon_{kl}^{\text{aux}}$, then $\sigma_{ij,1}^{\text{aux}}\varepsilon_{ij}$ can be expressed by

$$\sigma_{ij,1}^{\text{aux}}\varepsilon_{ij} = (C_{ijkl}(\boldsymbol{x})\varepsilon_{kl}^{\text{aux}})_{,1}\varepsilon_{ij} = (C_{ijkl,1}(\boldsymbol{x})\varepsilon_{kl}^{\text{aux}} + C_{ijkl}(\boldsymbol{x})\varepsilon_{kl,1}^{\text{aux}})\varepsilon_{ij} \tag{30}$$

and the expression $\sigma_{ij,1}\varepsilon_{ij}^{\text{aux}}$ is given by

$$\sigma_{ij,1}\varepsilon_{ij}^{\text{aux}} = (C_{ijkl}(\boldsymbol{x})\varepsilon_{kl})_{,1}\varepsilon_{ij}^{\text{aux}} = (C_{ijkl,1}(\boldsymbol{x})\varepsilon_{kl} + C_{ijkl}(\boldsymbol{x})\varepsilon_{kl,1})\varepsilon_{ij}^{\text{aux}}. \tag{31}$$

Substituting Eqs. (30) and (31) into (29) and using the equality of Eqs. (26)–(28), one obtains

$$M = \int_A \left\{(\sigma_{ij}^{\text{aux}}u_{i,1} + \sigma_{ij}u_{i,1}^{\text{aux}}) - \sigma_{ik}^{\text{aux}}\varepsilon_{ik}\delta_{1j}\right\}q_{,j}\,\mathrm{d}A + \int_A \left\{\sigma_{ij,j}^{\text{aux}}u_{i,1} + \rho\ddot{u}_i u_{i,1}^{\text{aux}} - C_{ijkl,1}\varepsilon_{kl}^{\text{aux}}\varepsilon_{ij}\right\}q\,\mathrm{d}A, \tag{32}$$

where $\sigma_{ij,j}^{\text{aux}}u_{i,1}$ appears due to the non-equilibrium condition of the auxiliary fields. Notice that $\sigma_{ij,j}^{\text{aux}}u_{i,1}$ and $C_{ijkl,1}\varepsilon_{kl}^{\text{aux}}\varepsilon_{ij}$ account for material non-homogeneity, while $\rho\ddot{u}_i u_{i,1}^{\text{aux}}$ represents dynamic effects. If dynamic effects are ignored, this equation reduces to the interaction integral for the static non-homogeneous material case derived by Kim and Paulino (2005).

4.3. Numerical implementation

The actual fields such as displacements, strains and stresses are evaluated globally by means of the FEM, while the auxiliary fields and SIFs are local quantities. Thus, transformation is unavoidable to obtain SIFs. In this work, the M-integral given by Eq. (32) is first computed globally to utilize the actual fields without any transformation and then transformed into the local system to obtain the SIFs.

The global M-integral quantities are evaluated as ($m = 1, 2$)

$$\begin{aligned}(M_m)^{\text{g}} = &\int_A \left\{(\sigma_{ij}^{\text{aux}}u_{i,m} + \sigma_{ij}u_{i,m}^{\text{aux}}) - \sigma_{ik}^{\text{aux}}\varepsilon_{ik}\delta_{mj}\right\}\frac{\partial q}{\partial X_j}\,\mathrm{d}A \\ &+ \int_A \left\{\sigma_{ij,j}^{\text{aux}}u_{i,m} + \rho\ddot{u}_i u_{i,m}^{\text{aux}} - C_{ijkl,m}\varepsilon_{kl}^{\text{aux}}\varepsilon_{ij}\right\}q\,\mathrm{d}A,\end{aligned} \tag{33}$$

where superscript "g" means global coordinate and X denotes the global coordinate system. Detailed explanation on the transformation of auxiliary fields from local to global coordinates is presented in Appendix A (see Fig. 4).

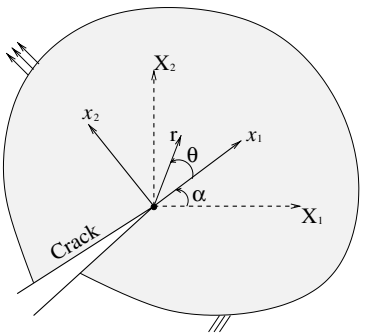

Fig. 4. Local (x_1, x_2) and global (X_1, X_2) coordinate systems.

The local M-integral quantities are evaluated as

$$M_{\text{local}} = (M_1)^{\text{g}} \cos\theta + (M_2)^{\text{g}} \sin\theta, \tag{34}$$

which is used to compute SIFs (see Section 4.4).

4.4. Extraction of SIFs

The actual and auxiliary relationship between J and mixed mode SIFs are, respectively

$$J_{\text{local}} = \frac{K_{\text{I}}^2 + K_{\text{II}}^2}{E^*_{\text{tip}}}, \tag{35}$$

$$J^{\text{aux}}_{\text{local}} = \frac{(K_{\text{I}}^{\text{aux}})^2 + (K_{\text{II}}^{\text{aux}})^2}{E^*_{\text{tip}}}, \tag{36}$$

where

$$E^*_{\text{tip}} = \begin{cases} E_{\text{tip}} & \text{plane stress,} \\ E_{\text{tip}}/(1-\upsilon^2_{\text{tip}}) & \text{plane strain.} \end{cases} \tag{37}$$

For the superimposed fields of actual and auxiliary fields, the relationship between J and SIFs of actual and auxiliary field is obtained as

$$J^s_{\text{local}} = \frac{(K_{\text{I}} + K_{\text{I}}^{\text{aux}})^2 + (K_{\text{II}} + K_{\text{II}}^{\text{aux}})^2}{E^*_{\text{tip}}} = J_{\text{local}} + J^{\text{aux}}_{\text{local}} + M, \tag{38}$$

where

$$M_{\text{local}} = \frac{2}{E^*_{\text{tip}}}(K_{\text{I}}K_{\text{I}}^{\text{aux}} + K_{\text{II}}K_{\text{II}}^{\text{aux}}). \tag{39}$$

By means of a judicious choice of auxiliary mode I and mode II SIFs, the SIFs of actual fields are decoupled and determined as

$$K_{\text{I}} = \frac{E^*_{\text{tip}}}{2} M_{\text{local}} \quad (K_{\text{I}}^{\text{aux}} = 1,\ K_{\text{II}}^{\text{aux}} = 0), \tag{40}$$

$$K_{\text{II}} = \frac{E^*_{\text{tip}}}{2} M_{\text{local}} \quad (K_{\text{I}}^{\text{aux}} = 0,\ K_{\text{II}}^{\text{aux}} = 1). \tag{41}$$

The relationship between SIFs and M-integral, i.e., Eqs. (40) and (41), is identical with those for homogeneous materials (Yau et al., 1980), except that the material properties are sampled at the crack tip location for non-homogeneous materials.

5. Verification

In this section, three cracked bodies of either homogeneous or non-homogeneous materials are analyzed to verify the M-integral implementation. The first problem is an unbounded non-homogeneous elastic medium containing an arbitrarily oriented crack. Analytical mixed-mode SIFs (Konda and Erdogan, 1994) are compared with present numerical results to verify the M-integral implementation for the static non-homogeneous

case. The second problem is a homogeneous edge-cracked semi-infinite plate under dynamic loading. Analytical mixed-mode DSIFs (Lee and Freund, 1990) are used as reference solution to verify the M-integral implementation for dynamic loading of homogeneous cracked specimen. The last problem is a non-homogeneous edge-cracked semi-infinite plate under dynamic loading. In order to verify the M-integral implementation for the dynamic non-homogeneous case, an ABAQUS user-subroutine (UMAT) (ABAQUS, 2004; Buttlar et al., 2005) and the DCT are employed to account for material non-homogeneity and to compute SIFs, respectively.

5.1. Non-homogeneous unbounded plate with an arbitrarily oriented crack

Konda and Erdogan (1994) obtained mixed-mode SIFs for an unbounded non-homogeneous elastic medium containing an arbitrarily oriented crack by solving integral equations. A finite plate, which is large relative to a crack length $2a = 8$, is chosen with width $2W = 80$ and height $2H = 80$, as illustrated in Fig. 5(a). Fig. 5(b)–(d) shows the whole mesh configuration, crack tip region and three different contours, respectively.

Young's modulus varies exponentially along the x-direction with a function, $E(x) = \overline{E}e^{\beta x}$, and a constant Poisson's ratio of 0.3 is used. Due to the material gradient for the fixed-grip loading, the applied load is equal to $\sigma_{22}(x, 40) = \bar{\varepsilon}\overline{E}e^{\beta X}$ where $\bar{\varepsilon}$ and $\overline{E}$ are equal to 1. Displacement boundary conditions, $u_2 = 0$ for

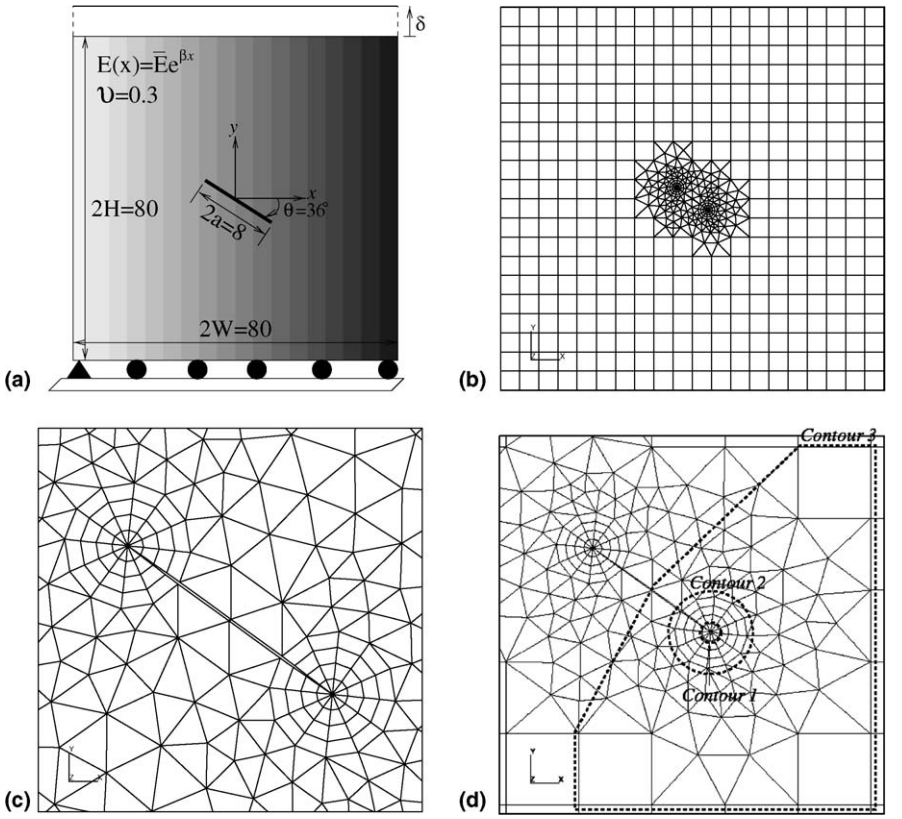

Fig. 5. Non-homogeneous unbounded plate: (a) geometry, boundary conditions and material properties; (b) mesh configuration for the whole geometry; (c) mesh details for the crack tip (12 sectors and 4 rings); (d) 3 different contours.

Table 1
Normalized SIFs at the right crack tip for 3 different contours ($\beta a = 0.5$ and $\theta/\pi = 0.32$)

	Contour 1	Contour 2	Contour 3
K_I	0.9270	0.9225	0.9224
K_{II}	−0.5446	−0.5492	−0.5502

Table 2
Comparison of normalized SIFs at both crack tips between the present solution, and the current analytical solution and numerical results ($\beta a = 0.5$ and $\theta/\pi = 0.32$)

References	Left crack tip		Right crack tip	
	K_I	K_{II}	K_I	K_{II}
Konda and Erdogan (1994)	0.925	−0.548	0.460	−0.365
Present	0.9225	−0.5492	0.4560	−0.3623
Kim and Paulino (2003b)	0.9224	−0.5510	0.4559	−0.3621
Dolbow and Gosz (2000)	0.930	−0.560	0.467	−0.364

the bottom edge and $u_1 = 0$ for the left bottom node, are prescribed. Plane stress elements are used for the bulk elements which consist of 446 Q8 and 274 T6 elements. Ratios $\beta a = 0.5$ and $\theta/\pi = 0.32$ are chosen.

Table 1 shows normalized K_I and K_{II} for three different contours, demonstrating domain independence of the M-integral. The mixed mode SIFs are normalized with respect to $K_0 = \bar{\varepsilon}\bar{E}\sqrt{\pi a}$. Table 2 compares the present normalized SIFs with the analytical solutions obtained by Konda and Erdogan (1994), and numerical results obtained by Dolbow and Gosz (2000) using X-FEM and by Kim and Paulino (2003b) using the I-FRANC2D finite element code. Dolbow and Gosz (2000) and Kim and Paulino (2003b) used the M-integral to obtain SIFs. Good agreement exists between the present numerical results and the analytical solutions, which have a maximum difference of 0.8%.

5.2. Homogeneous edge cracked semi-infinite plate

Lee and Freund (1990) evaluated mixed-mode DSIFs for an edge-cracked semi-infinite plate under impact loading using linear superposition of obtainable stress wave solutions. During the period from initial loading until the first scattered waves at the crack tip are reflected, the mixed-mode SIF history was determined. Belytschko (1995) studied this problem numerically and evaluated DSIFs using the EFG method.

A finite plate with width $W = 0.2$ m, height $H = 0.3$ m and crack length $a = 0.05$ m is chosen, as illustrated in Fig. 6. The velocity, $v = 6.5$ m/s, is imposed on the upper half of the left boundary and no other boundary conditions are prescribed (see Fig. 6(a)). The material properties of steel are chosen as $E = 200$ GPa, $\rho = 7850$ kg/m^3 and $\nu = 0.25$. The corresponding wave speeds are

$$C_d = \sqrt{\frac{E(1-\nu)}{\rho(1+\nu)(1-2\nu)}} = 5529.3 \text{ m/s}, \tag{42}$$

$$C_s = \sqrt{\frac{E}{2\rho(1+\nu)}} = 3192 \text{ m/s}, \tag{43}$$

$$C_R \approx 0.928 c_s \approx 2962 \text{ m/s}, \tag{44}$$

where C_d, C_s and C_R are the longitudinal wave, shear wave, and *Rayleigh* wave speeds (Fung, 1965), respectively. Plane strain condition is used with a full integration scheme, and the average acceleration method is used with a time step of $\Delta t = 0.4$ μs. Consistent mass matrix is used for the mass matrix formulation.

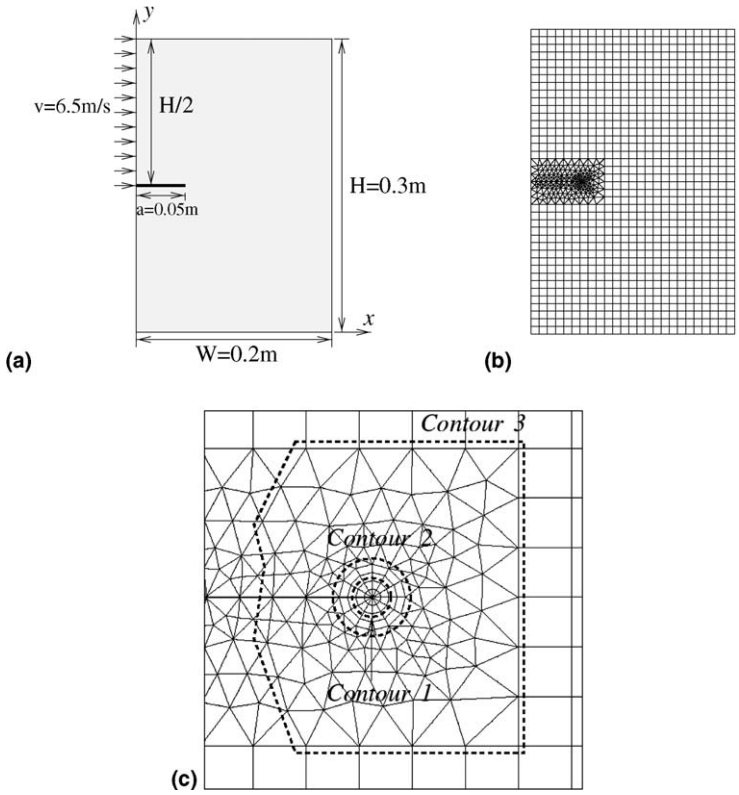

Fig. 6. Edge cracked semi-infinite plate: (a) geometry and boundary conditions; (b) mesh configuration for the whole geometry; (c) close up of crack tip (12 sectors and 4 rings) and 3 different contours.

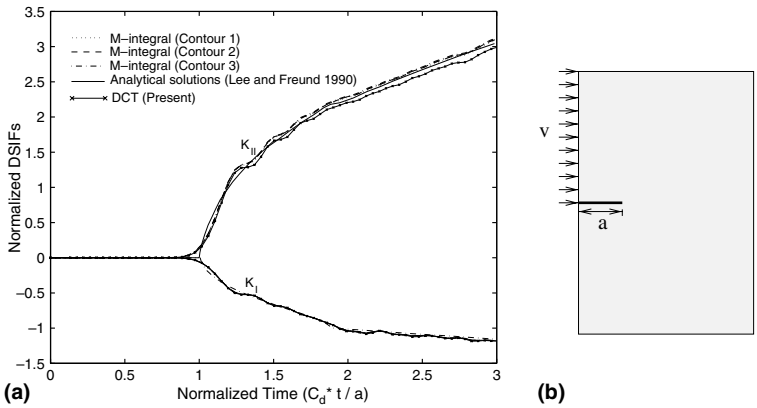

Fig. 7. Comparison of the numerical results for the M-integral (considering three different contours) and the DCT with the analytical solutions ($K_{\mathrm{I}}(t)$ and $K_{\mathrm{II}}(t)$).

The present numerical results using the M-integral and DCT are compared with the analytical solutions (Lee and Freund, 1990) in terms of normalized mixed-mode DSIFs and normalized time in Fig. 7. To

ensure domain independence of the M-integral, numerical results for three different contours are plotted together in Fig. 7. The abscissa is time normalized with respect to the crack length and dilatational wave speed, and the ordinate is DSIFs normalized as

$$\frac{E\mathrm{v}\sqrt{a/\pi}}{2C_{\mathrm{d}}(1-\nu^2)}. \tag{45}$$

The history of DSIFs is plotted from the initial loading until the first wave scattered at the crack tip bounces back from the boundary. As illustrated, the present numerical results using the M-integral and the analytical solutions agree well. Besides, the DCT yields $K_{\mathrm{I}}(t)$ values identical to analytical solutions. However, there is some discrepancy between the $K_{\mathrm{II}}(t)$ values for the DCT and the analytical solutions. Similar observation was noted by Kim and Paulino (2002b) for static problems involving cracks in FGMs. For both $K_{\mathrm{I}}(t)$ and $K_{\mathrm{II}}(t)$, the magnitude of DSIFs increases gradually, due to the instantaneous velocity. The compressive waves and relatively large shear waves generated from the applied velocity induce the negative $K_{\mathrm{I}}(t)$ and positive $K_{\mathrm{II}}(t)$ as shown in Fig. 7. Notice that since the numerical results for three different contours overlap each other, domain independence is demonstrated numerically.

5.3. Non-homogeneous edge cracked semi-infinite plate

In the previous example, the M-integral implementation for dynamic homogeneous case was verified by comparing the present numerical results with the analytical solutions by Lee and Freund (1990). In this section, the UMAT (ABAQUS, 2004) is used to incorporate material gradations of Young's modulus under dynamic loading, and the DCT (Shih et al., 1976) is employed to compute SIFs. The UMAT and DCT are adopted to verify the M-integral implementation for the dynamic non-homogeneous case. The UMAT was developed to analyze pavement systems which are graded due to temperature gradients and aging related stiffness gradients (Buttlar et al., 2005). In the UMAT, graded elements are implemented by means of direct sampling of properties at the Gauss points of the element (Kim and Paulino, 2002a; Santare and Lambros, 2000).

The same geometry and boundary conditions shown in Fig. 6(a) are used. The mass density and Poisson's ratio are $\rho = 7850\ \mathrm{kg/m^3}$ and $\nu = 0.25$, respectively. The elastic modulus varies exponentially along the x-direction as follows:

$$E(x) = E(0)\mathrm{e}^{\beta x}, \quad \beta = \frac{1}{W}\log\left(\frac{E(W)}{E(0)}\right), \tag{46}$$

where $W = 0.2$ m, $E(0) = 100$ GPa, $E(W) = 300$ GPa and β is the material non-homogeneity parameter. The material properties at the crack tip are $E = 131.6$ GPa, $\rho = 7850\ \mathrm{kg/m^3}$ and $\nu = 0.25$. Plane strain elements are used with 3×3 Gauss quadrature. The average acceleration method is adopted with a time step of $\Delta t = 0.4\ \mu$s and consistent mass matrix is employed.

Fig. 8 illustrates the variation of DSIFs with time and compares the DSIFs using both the M-integral and the DCT from the present results with those using the DCT from ABAQUS. The abscissa and ordinate indicate time and DSIFs, respectively. DSIFs of $K_{\mathrm{I}}(t)$ and $K_{\mathrm{II}}(t)$ using the DCT for both the present and ABAQUS results are within plotting accuracy. The two different numerical schemes, i.e., the M-integral and the DCT, yield almost identical $K_{\mathrm{I}}(t)$ values and slightly different $K_{\mathrm{II}}(t)$ values, similarly to the homogeneous case (see Fig. 7). This demonstrates that field quantities, i.e., displacements, strains and stresses, and the computed DSIFs using the M-integral for cracked non-homogeneous media under dynamic loading are computed correctly using the research code developed.

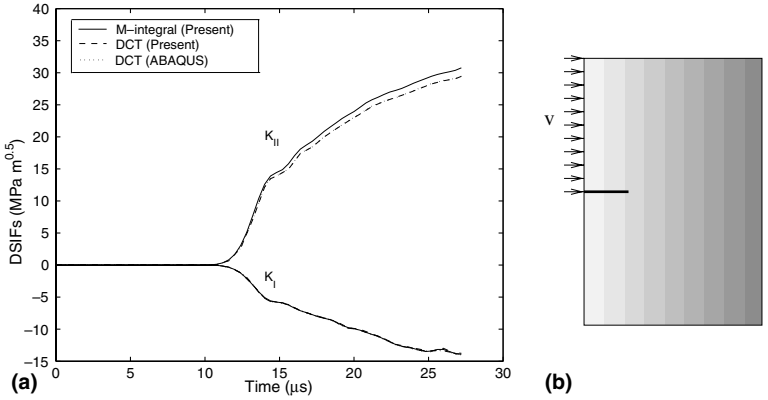

Fig. 8. Comparison of numerical results between the M-integral and the DCT.

6. Numerical examples

With the code verified, various problems are examined to evaluate DSIFs for homogeneous and non-homogeneous materials and to explore fracture behavior for different material profiles. In this chapter, the following problems are considered:

- Homogeneous center cracked tension (CCT) specimen, which is a pure mode I problem.
- Non-homogeneous CCT specimen with mixed-mode crack behavior.
- Homogeneous and non-homogeneous rectangular plate with an inclined crack.
- Homogeneous and non-homogeneous rectangular plate with cracks emanating from a circular hole.

In the examples, domain independence is assessed and the present numerical results are compared with reference solutions. The dynamic fracture behavior is investigated for different material gradations considering the influence of the time step on DSIFs, the relation between initiation time and the domain size, and the contribution of each distinct term consisting in the M-integral. The standard average acceleration method and consistent mass matrix are used in all the examples (Newmark, 1959; Hughes, 1987).

6.1. Homogeneous CCT specimen

This problem was first examined by Chen (1975) and since then, it has been considered as a benchmark problem. Chen (1975) determined mode I SIFs for a CCT specimen under step loading using a time dependent Lagrangian finite difference method (FDM). In his work, DSIFs were determined using the relation between stresses and SIFs around the crack tip.

Chen's (1975) problem has been studied by many researchers. Brickstad (1983) utilized the relation between SIFs and crack opening displacement (COD) to obtain DSIFs. Murti and Valliappan (1986) employed the finite element method to determine DSIFs using the DCT. Lin and Ballmann (1993) revisited Chen's problem using the FDM. They employed a greater number of finite difference cells and obtained slightly different numerical results. Dominguez and Gallego (1992) computed DSIFs using the BEM with quarter-point elements (QPEs). Sladek et al. (1997, 1999) used the $\widehat{J}$ integral to determine DSIFs in the BEM context.

6.1.1. Problem description

Consider a rectangular finite plate of width $2W = 20$ mm and height $2H = 40$ mm, with a center crack of length $2a = 4.8$ mm. Geometry, boundary conditions, finite element discretization, and three different

M-integral domain contours are illustrated in Fig. 9. The total mesh (see Fig. 9(b)) consists of 816 Q8 and 142 T6 2D plane strain elements. Notice that 8 T6 elements and 24 Q8 elements, which consist of four rings and eight sectors, are employed as the crack tip template and lead to sufficient mesh refinement around the crack tips. The external force, $p(t)$, is applied instantaneously to both top and bottom edges with a step function, as shown in Fig. 10. No other boundary conditions are prescribed. Young's modulus, mass den-

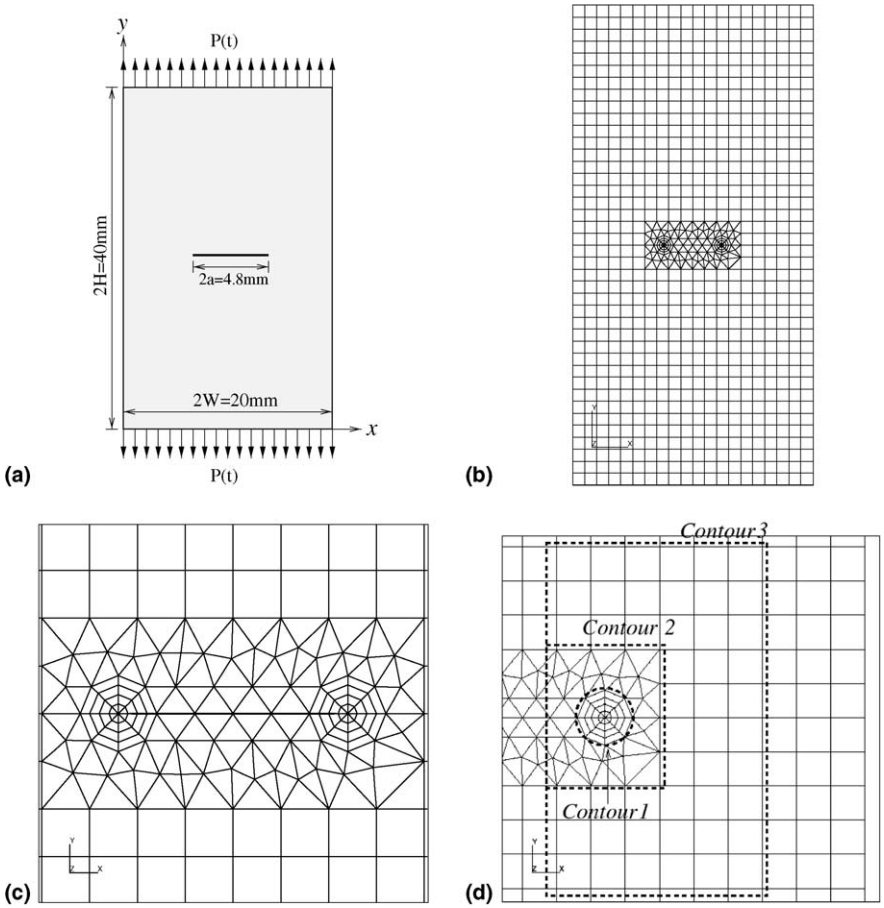

Fig. 9. Benchmark CCT specimen: (a) geometry and boundary conditions; (b) mesh configuration for whole geometry; (c) mesh detail for the crack tip regions (8 sectors and 4 rings); (d) domain contours.

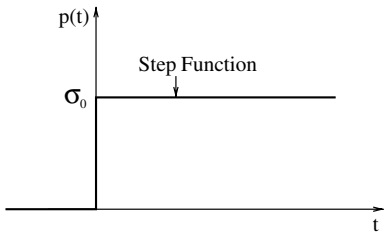

Fig. 10. Applied load versus time (step function).

sity and Poisson's ratio are 199.992 GPa, 5000 kg/m^3 and 0.3, respectively, and the corresponding wave speeds are

$$C_d = \sqrt{\frac{E(1-v)}{\rho(1+v)(1-2v)}} = 7.34 \text{ mm}/\mu\text{s}, \tag{47}$$

$$C_s = \sqrt{\frac{E}{2\rho(1+v)}} = 3.92 \text{ mm}/\mu\text{s}, \tag{48}$$

$$C_R \approx 0.928 c_s \approx 3.63 \text{ mm}/\mu\text{s}, \tag{49}$$

where C_d, C_s and C_R are the longitudinal wave, shear wave, and *Rayleigh* wave speeds (Fung, 1965), respectively. A time step $\Delta t = 0.05$ μs and full integration scheme are employed.

6.1.2. Comparison between J and M-integrals

Rice proposed the *J*-integral which is equivalent to the energy release rate under static linear elastic conditions (Rice, 1968). Since then, this method has been widely used and has been the basis of new methods proposed by many researchers. For instance, the *J*-integral can be decomposed to evaluate mixed mode SIFs (Kishimoto et al., 1980; Fedelinski et al., 1994; Bui, 1983). Under dynamic loading conditions, it is necessary to include dynamic terms in order to obtain domain independent DSIFs (Wu et al., 2002; Moran and Shih, 1987). Owing to significance of the *J*-integral in fracture mechanics, we implemented Eq. (14) in the code employing the equivalent domain integral formulation (EDI) (Raju and Shivakumar, 1990) and used the *J*-integral to verify the implementation of the *M*-integral for mode I problem.

A comparison of numerical results between using the *J*-integral and *M*-integral in terms of DSIFs is performed. Fig. 11 compares DSIFs obtained using the *J* and the *M*-integrals. The time is normalized with respect to the dilatational wave speed (c_d), and the DSIFs are normalized with respect to

$$K_s = \sigma_0(\sqrt{\pi a}), \tag{50}$$

where the σ_0 is the magnitude of the applied stress and a is half of the total crack length. Up to the normalized time T_1 of 4.3 in Fig. 11, the two numerical results match within 0.02%, which is expected because the *M*-integral is based on the *J*-integral. However, after the time T_1 both schemes yield nearly equal

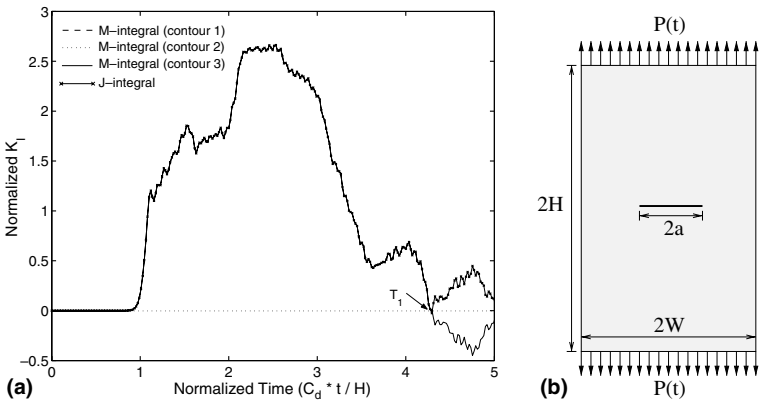

Fig. 11. Numerical comparison between the *J*-integral and the *M*-integral. Notice that the numerical results for three different contours are plotted together to illustrate the domain independence.

magnitude but they are opposite in sign as illustrated in Fig. 11. Because J represents an energy which is always positive, the calculation of SIFs from J values, which follows:

$$K = \sqrt{JE^*}, \tag{51}$$

always yields a positive value of $K_I(t)$. This fact indicates that the J-integral may have limitations for dynamic problems because transient DSIFs often oscillate between positive and negative values. Here the negative mode I SIF simply indicates crack closure.

Furthermore, the present numerical results for the three different contours are compared each other in Fig. 11 to illustrate domain independence. To evaluate domain independence numerically, three different contours are selected, as illustrated in Fig. 9(d). The similarity of numerical results for the three different contours demonstrate numerical domain independence.

6.1.3. Comparison of present results with a numerical reference solution

Lin and Ballmann (1993) revisited Chen's problem using the FDM and obtained DSIFs utilizing the relation between SIFs and stress. Fig. 12 compares the present numerical results with those of Lin and Ballmann (1993). A software named as DigXY was used to extract numerical values from graphical data in reference (Lin and Ballmann, 1993).

Overall, there is good agreement between the present numerical results and the reference solution. The reference solution shows a theoretical normalized initiation time of 1 as illustrated in Fig. 12 because the step function is adopted for external loading. The present numerical results indicate an initiation time smaller than the theoretical value. However, the numerical initiation time approaches the theoretical value as the time step is decreased, which will be presented below (see Section 6.1.4). For the first peak, both results show a similar magnitude and corresponding time.

6.1.4. Comparison of theoretical initiation time and first peak

In this section, two important time locations, the initiation time and the first peak, during transient responses, are discussed by comparing the present numerical values with theoretical ones. The theoretical initiation time corresponds to the time necessary for a dilatational wave induced by external forces to reach a crack tip location, and in this case it equals H/c_d. Ideally, the numerical initiation time should coincide with the theoretical initiation time. In reality, numerical initiation values precede the theoretical values. For this problem, the normalized initiation time of the numerical results is 0.9 when time step 0.05 μs is adopted, and the normalized theoretical initiation time is 1. Through numerical simulations, we observe that as

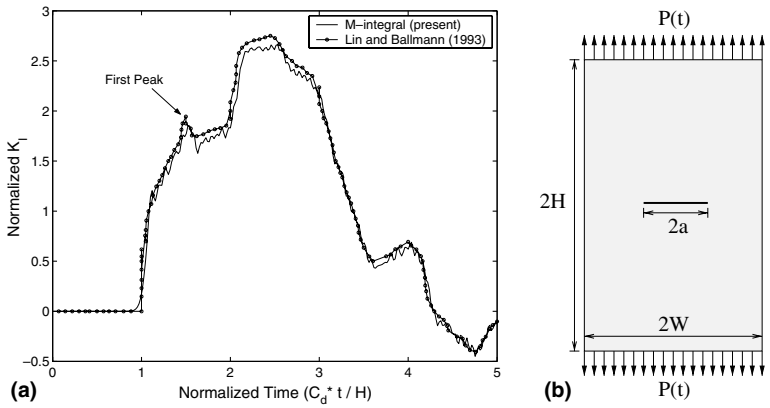

Fig. 12. Comparison between the present numerical results and the reference solution by Lin and Ballmann (1993).

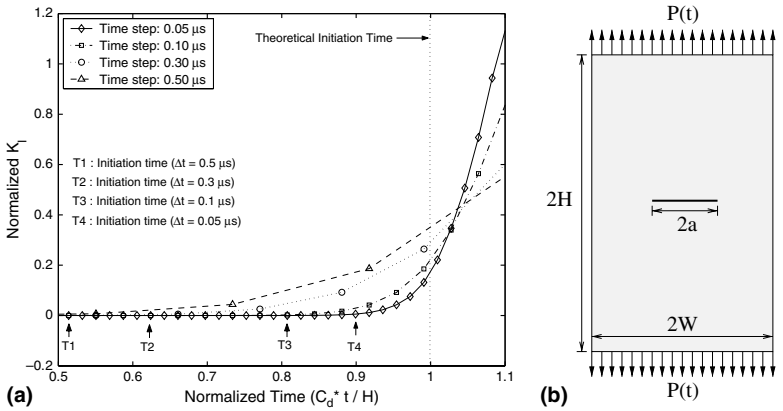

Fig. 13. Initiation time for 4 different time steps.

the time step decreases, the numerical initiation time approaches the theoretical value of 1 in Fig. 13. The normalized $K_I(t)$ for different time steps (0.05 μs, 0.1 μs, 0.3 μs and 0.5 μs) is plotted versus the normalized time in Fig. 13.

The first peak, indicated in Fig. 12, occurs in this problem when dilatational waves reach the crack tip, and generated *Rayleigh* waves travel to the opposite crack tip. At that instant, the *Rayleigh* waves cause compression at the crack tip and thus reduce the $K_I(t)$ values. The normalized theoretical time for this event is 1.485 and the present numerical value is 1.523 for a time step of $\Delta t = 0.05$ μs. There is reasonably good agreement between these numbers with a relative error less than 3%.

6.1.5. Sensitivity of numerical results with respect to time step size

For step loading, transient DSIFs are highly influenced by time step increment because the waves induced by this loading have a significant influence on crack tip fields, whereas for ramp loading, the crack tip fields are influenced primarily by the remote load. In the ramp loading, the load is always increasing with time and, as a consequence, the magnitude of SIFs increases monotonically with time and shows little variation due to propagating waves. Therefore, SIFs are not very sensitive to the time step increment for ramp loading.

Four different time steps, 0.05 μs, 0.1 μs, 0.3 μs and 0.5 μs, are chosen to investigate the influence of time step on the DSIFs for step loading. As illustrated in Fig. 14, numerical results are highly influenced by the time step. The abscissa and ordinate represent normalized time and normalized $K_I(t)$, respectively. As the time step decreases, the numerical results appear to converge. For the larger time steps, the difference between numerical results is especially pronounced near the peaks. This result indicates that for large time steps, the transient response cannot be captured accurately.

6.1.6. Discussion of M-integral terms

The M-integral based on the non-equilibrium formulation is given by Eq. (32), i.e.,

$$M = \int_A \left\{ (\sigma_{ij}^{\text{aux}} u_{i,1} + \sigma_{ij} u_{i,1}^{\text{aux}}) - \sigma_{ik}^{\text{aux}} \varepsilon_{ik} \delta_{1j} \right\} q_{,j} \, \mathrm{d}A + \int_A \left\{ -C_{ijkl,1} \varepsilon_{kl}^{\text{aux}} \varepsilon_{ij} + \sigma_{ij,j}^{\text{aux}} u_{i,1} + \rho \ddot{u}_i u_{i,1}^{\text{aux}} \right\} q \, \mathrm{d}A. \tag{52}$$

The above expression consists of various terms which accounts for dynamic effects and material non-homogeneity. Now, we will investigate and discuss the contribution of each term of the M-integral and its domain independence. Let us define

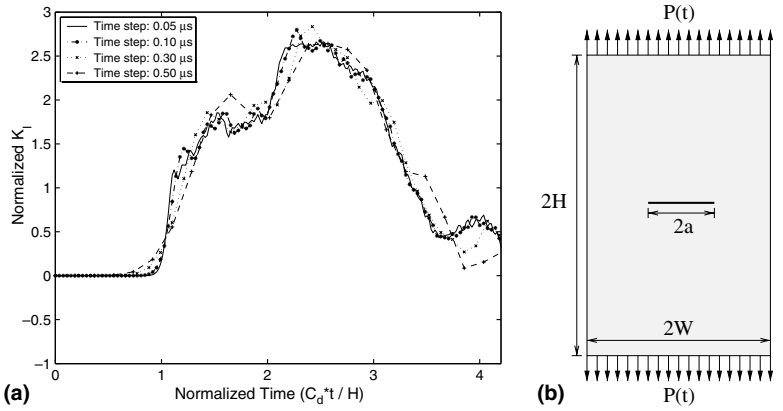

Fig. 14. Normalized $K_{\mathrm{I}}(t)$ at the right crack tip for 4 different time steps: 0.05 μs, 0.1 μs, 0.3 μs and 0.5 μs.

$$\text{Term 1} = \int_A \sigma_{ij}^{\text{aux}} u_{i,1} q_{,j}\, \mathrm{d}A, \tag{53}$$

$$\text{Term 2} = \int_A \sigma_{ij} u_{i,1}^{\text{aux}} q_{,j}\, \mathrm{d}A, \tag{54}$$

$$\text{Term 3} = -\int_A \sigma_{ik}^{\text{aux}} \varepsilon_{ik} \delta_{1j} q_{,j}\, \mathrm{d}A, \tag{55}$$

$$\text{Term 4} = -\int_A C_{ijkl,1} \varepsilon_{kl}^{\text{aux}} \varepsilon_{ij} q\, \mathrm{d}A, \tag{56}$$

$$\text{Term 5} = \int_A \sigma_{ij,j}^{\text{aux}} u_{i,1} q\, \mathrm{d}A, \tag{57}$$

$$\text{Term 6} = \int_A \rho \ddot{u}_i u_{i,1}^{\text{aux}} q\, \mathrm{d}A. \tag{58}$$

Terms 1, 2, and 3 are the same as those for homogeneous materials under quasi-static conditions. Terms 4 and 5 arise due to material non-homogeneity, and Term 6 is due to dynamic effects.

For this simulation, the contours shown in Fig. 9(d) are used. Contour 1 includes 8 T6 and 24 Q8 elements, contour 2 contains 54 T6 and 24 Q8 elements, and contour 3 has 54 T6 and 72 Q8 elements. Fig. 15(a)–(c) shows the contribution of each term to the normalized K_{I} using contours 1, 2, and 3, respectively. The abscissa and ordinate represent normalized time and normalized $K_{\mathrm{I}}(t)$, respectively. Terms 4 and 5 are not included in Fig. 15 because they are zero for homogeneous materials. For all contours, the contributions of Terms 1 and 2 are higher than those of the other terms. Terms 1, 2, and 3 follow the trend of the total K, whereas Term 6 oscillates. Two important phenomena are observed from this simulation. The first is the oscillatory nature of the contribution of Term 6 for different contours. The second is the relationship between initiation time and domain size.

For contour 1, illustrated in Fig. 15(a), the magnitude of Term 6 is small compared to that of other terms. But as the domain size increases (from contour 1 to contour 3), the magnitude of Term 6 increases overall as illustrated in Fig. 16. It turns out that even if Term 6, which accounts for dynamic effects, is relatively small compared to other terms, the influence of this term in obtaining DSIFs becomes significant as

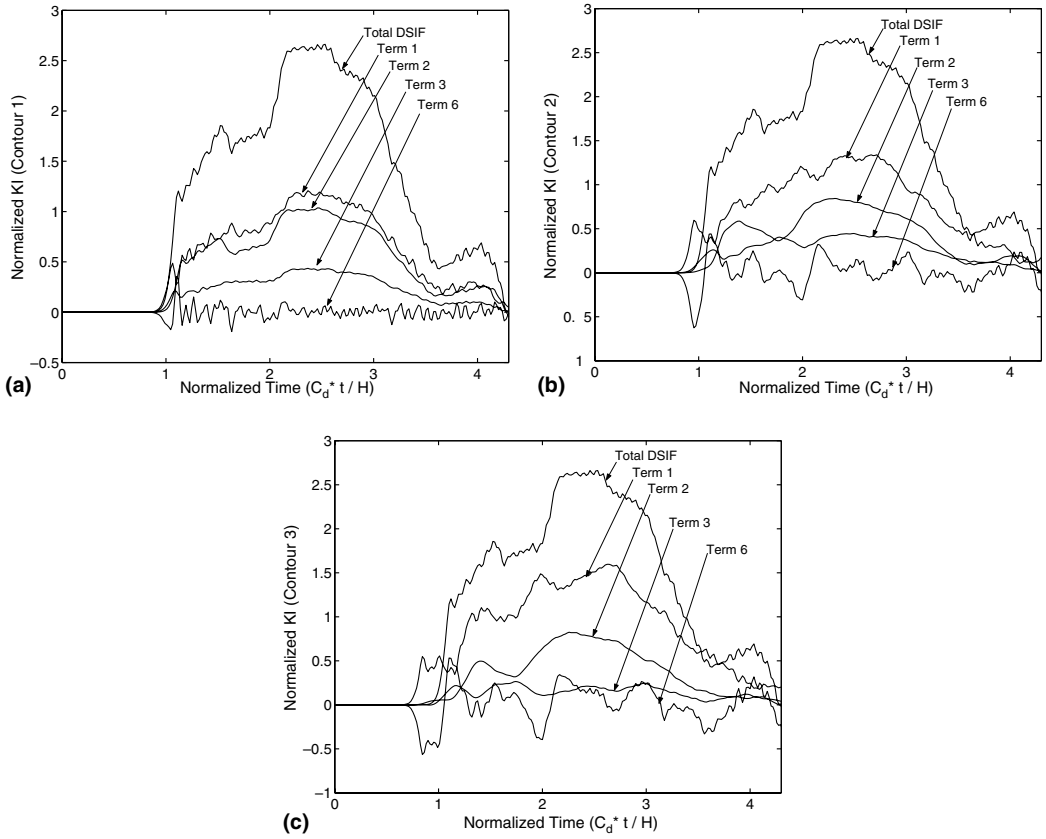

Fig. 15. Normalized $K_I(t)$ for three different contours: (a) contribution of each term for contour 1; (b) contribution of each term for contour 2; (c) contribution of each term for contour 3.

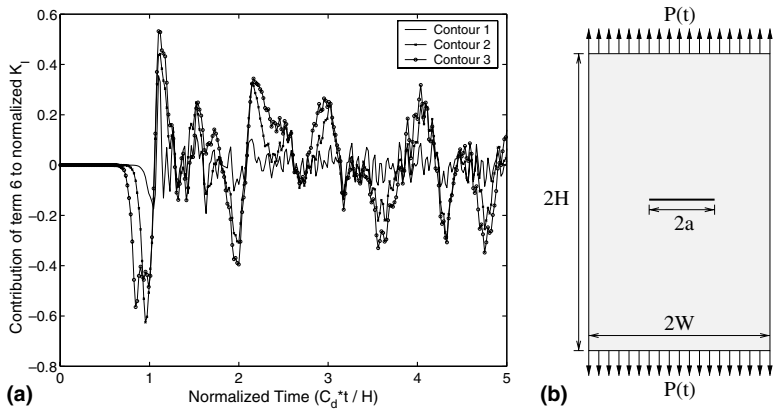

Fig. 16. Contribution of Term 6 to normalized DSIFs for three different contours.

the domain size increases. Therefore, this term must be taken into account to satisfy domain independence and to obtain correct DSIFs for dynamic problems.

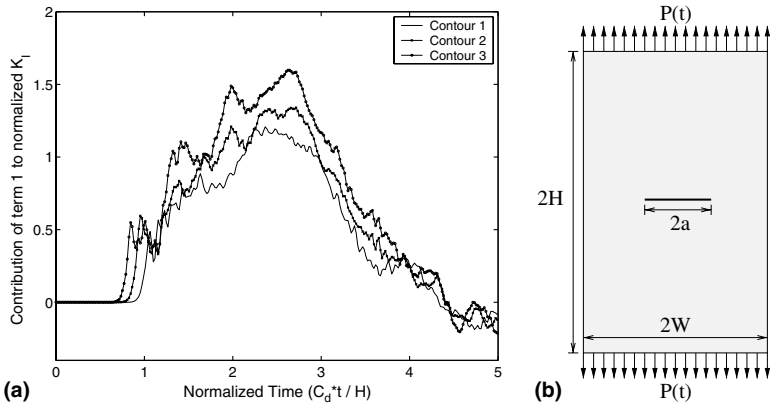

Fig. 17. Contribution of Term 1 to normalized DSIFs for three different contours.

Dilatational waves reach the boundary of larger domains earlier than the boundary of small domains. We now investigate initiation times of individual terms for different domain sizes. Fig. 15 shows the contribution of each term for the three contours. Because contour 1 is very small, the difference between the initiation time for each term and for the total DSIF is small (see Fig. 15(a)). However, for the larger contours 2 and 3 (see Fig. 15(b) and (c), respectively), it is clearly observed that Terms 1 and 6 initiate earlier than the total DSIF. Moreover, Terms 1 and 6 initiate earlier, as domain size increases, as shown in Figs. 17 and 16, respectively. However, the change of initiation time for the different domain sizes is not pronounced for Terms 2 and 3 (see Fig. 15). Notice that even if a few terms initiate earlier as the domain size increases, the initiation time of the total DSIF is independent of domain size, demonstrating domain independence (see Fig. 11).

6.2. Non-homogeneous CCT specimen

Dynamic fracture behavior of a homogeneous CCT specimen is examined thoroughly in Section 6.1. In this section, various material profiles are adopted to investigate fracture behavior in a non-homogeneous specimen. First, domain independence of DSIFs for non-homogeneous material is verified. Then, behavior of DSIFs at the right and left crack tips is explored.

Young's modulus and mass density vary exponentially, such that $E/\rho \equiv$ constant, as given by

$$E = E_{\mathrm{H}} \exp(\beta_1 x + \beta_2 y), \tag{59}$$

$$\rho = \rho_{\mathrm{H}} \exp(\beta_1 x + \beta_2 y), \tag{60}$$

where E_{H} and ρ_{H} are Young's modulus and mass density for homogeneous materials and β_1 and β_2 are non-homogeneity parameters along the x- and y-directions, respectively. When β_1 and β_2 are equal to zero, Eqs. (59) and (60) reflect homogeneous materials. A constant Poisson ratio of 0.3 is used. Plane strain elements with 3×3 Gauss quadrature and consistent mass matrices are adopted for the bulk elements. A time step is $\Delta t = 0.1$ μs. The geometry and the boundary conditions are identical to those of homogeneous specimen analyzed in Section 6.1.1. Notice again that no other boundary conditions are prescribed except for the external loading.

6.2.1. Domain independence for non-homogeneous materials

In this section, domain independence of the M-integral for non-homogeneous materials is demonstrated numerically. In order to employ severe material gradations, relatively high β values are chosen: $\beta_1 = 0.1$ and

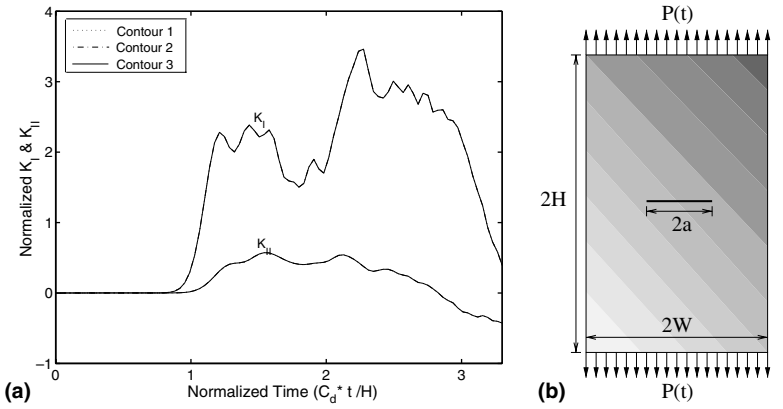

Fig. 18. Normalized DSIFs for three different contours.

$\beta_2 = 0.1$. Material properties vary simultaneously along both the x- and y-directions according to coordinate system shown in Fig. 9(a).

Fig. 18 shows DSIFs at the right crack tip for the same contours used in the homogeneous specimen (see Fig. 9(d)). The abscissa and ordinate are normalized by the homogeneous material constants, given by the dilatational wave speed of 7.34 mm/μs in Eq. (47) and the SIF in Eq. (50), respectively. Even with high material gradation, the normalized $K_{II}(t)$ is relatively small for this loading and geometry. The numerical results for the three different contours shown in Fig. 18 are identical, demonstrating domain independence for non-homogeneous materials.

6.2.2. Exponentially graded materials in the y-direction

In this section, we consider material properties that vary along the y-direction. The material gradation parameter β_1 is set to 0.0, and β_2 is chosen as 0.0, 0.05 and 0.1. Since material properties vary along the y-direction, the material properties are the same at both crack tips. The ratios of material properties between the bottom and top edges are 1.0, 7.4 and 54.6, which correspond to $\beta_1 = 0.0$, 0.05, and 0.1, respectively.

Fig. 19 shows mixed mode DSIFs at the right crack tip. The contour 3 shown in Fig. 9(d) is used to evaluate the M-integral. The abscissa indicates time normalized with respect to the homogeneous dilatational wave speed of 7.34 mm/μs in Eq. (47) and the ordinate indicates the DSIFs normalized as the homogeneous analytical SIF in Eq. (50). Since material gradations vary along the y-direction, $K_I(t)$ is identical at both crack tips, while the magnitude of $K_{II}(t)$ at the left crack tip is equal in magnitude and opposite in sign to the value at the right crack tip. The initiation time at both crack tips remains the same for all cases of material gradations because the same exponential function describes Young's modulus and mass density. Values of $K_{II}(t)$, induced by material gradients, are more significant with increasing β, whereas the maximum magnitude of $K_I(t)$ is relatively insensitive to β. Nevertheless, the magnitude of $K_{II}(t)$ is relatively small compared to that of $K_I(t)$.

6.3. Rectangular plate with an inclined crack

Chen and Wilkins (1976) studied the problem of a rectangular plate with an inclined crack using the FDM and obtained results which have been questioned by several researchers. Murti and Valliappan (1986) investigated this problem using QPEs with the FEM. Dominguez and Gallego (1992), Fedelinski et al. (1994), and Sladek et al. (1999) investigated this problem using the BEM. Krysl and Belytschko (1999) and Tabiei and Wu (2003) explored the problem with the 3D EFG and the 3D FEM, respectively.

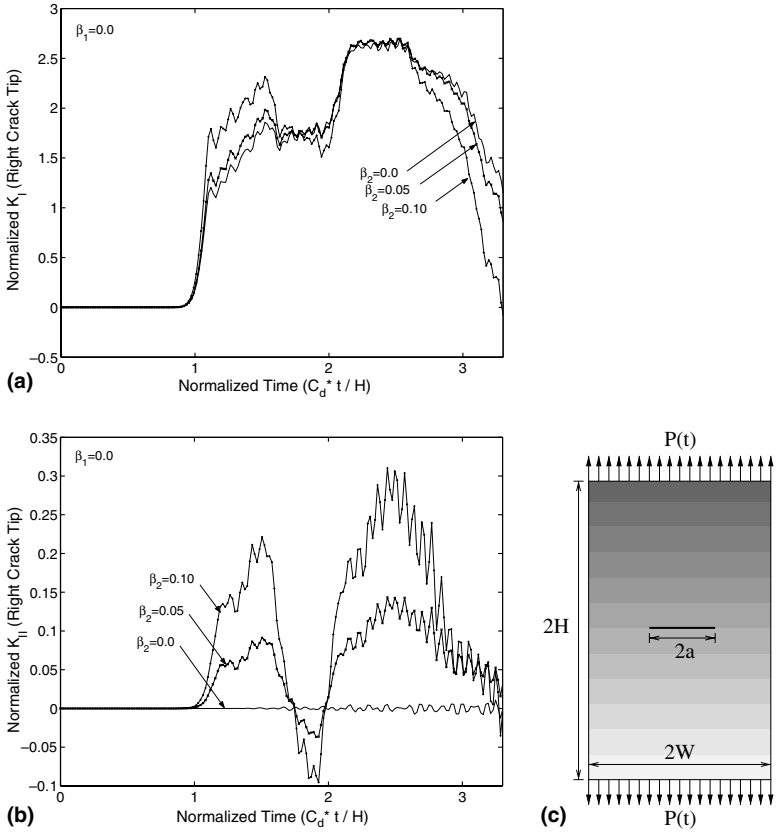

Fig. 19. DSIFs for different material gradations along the y-direction: (a) normalized $K_{\mathrm{I}}(t)$ at the right crack tip; (b) normalized $K_{\mathrm{II}}(t)$ at the right crack tip; (c) functionally graded CCT specimen.

Consider an inclined crack of length $2a = 14.14$ mm in a rectangular plate of width $2W = 30$ mm and height $2H = 60$ mm, as shown in Fig. 20(a). Fig. 20(b) and (c) illustrate the mesh for the whole geometry, and the four contours employed at each crack tip. The entire mesh consists of 206 Q8 and 198 T6 elements. Contour 1 includes only 8 T6 elements, contour 2 encloses 8 T6 and 24 Q8 elements, contour 3 contains 31 T6 and 24 Q8 elements, and contour 4 has 77 T6 and 26 Q8 elements. To obtain a reasonable mesh resolution near the crack tips, 4 rings and 8 sectors of elements are used. The external force, $p(t)$, is applied instantaneously to both the top and bottom edges with a step function (see Fig. 10). No other boundary conditions are prescribed.

For the non-homogeneous case, Young's modulus and mass density vary exponentially along the x- and y-directions, such that $E/\rho \equiv$ constant, according to

$$E = E_{\mathrm{H}} \exp(\beta_1 x + \beta_2 y), \tag{61}$$

$$\rho = \rho_{\mathrm{H}} \exp(\beta_1 x + \beta_2 y), \tag{62}$$

where E_{H} and ρ_{H} are Young's modulus and mass density for homogeneous material, and β_1 and β_2 are the material non-homogeneity parameters that describe material gradation. When β_1 and β_2 equal zero, homogeneous material properties are recovered. A constant Poisson's ratio of 0.3 is employed. Plane strain elements with 3×3 Gauss quadrature are used. A time step is $\Delta t = 0.1$ μs.

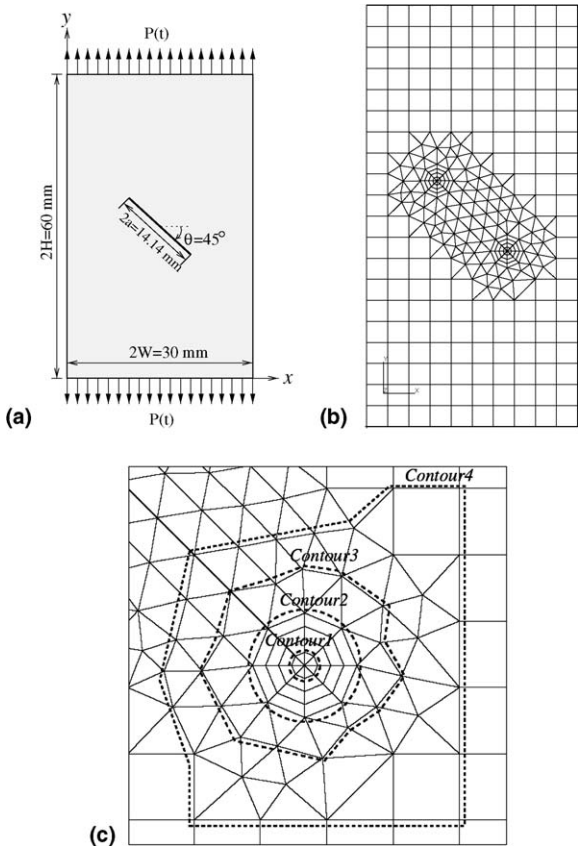

Fig. 20. Rectangular plate with an inclined crack: (a) geometry and boundary conditions; (b) mesh configuration for whole geometry; (c) domain contours.

In this section, we compare the present numerical results with current available reference solutions for homogeneous materials. Then, material gradations which vary along the x-direction are adopted to investigate dynamic fracture behavior in terms of DSIFs for non-homogeneous materials. The influence of domain sizes and the contribution of each term in the M-integral are explored.

6.3.1. Homogeneous rectangular plate

Here, the present numerical results are compared with available reference solutions for the homogeneous material case. With parameters β_1 and β_2 set to zero, the following homogeneous material properties are employed:

$$E = 199.992\ \text{GPa}, \quad \rho = 5000\ \text{kg/m}^3, \quad \nu = 0.3. \tag{63}$$

The corresponding wave speeds are given by Eqs. (47)–(49).

Fig. 21 shows a comparison between the present numerical results and the reference solutions by Fedelinski et al. (1994) who used a time-domain BEM, Dominguez and Gallego (1992) who used the dual BEM with the $\widehat{J}$ integral, and Murti and Valliappan (1986) who used FEM with QPEs. The abscissa indicates time. The ordinate indicates the DSIF normalized with respect to K_s given by Eq. (50).

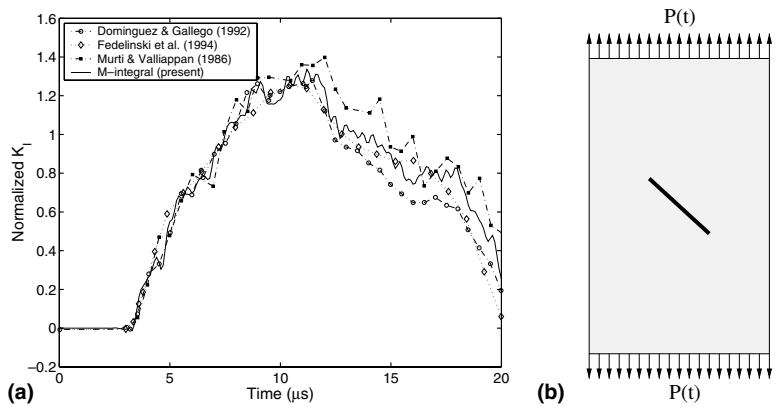

Fig. 21. Numerical comparison between the present results and the reference solutions (Murti and Valliappan, 1986; Dominguez and Gallego, 1992; Fedelinski et al., 1994).

The reference results plotted here are obtained from graphical data using special-purpose software. Up to 10 μs, the difference between the results is not significant. After that time, the discrepancy among the results becomes greater when the influence of reflected waves becomes significant. This implies that the various numerical schemes differently predict the transient fracture response which is highly influenced by propagating waves reflected from the boundary and crack surfaces. Up to 10 μs, the present results match well with the solution by Dominguez and Gallego (1992), and afterwards, the present results are within the range of the other solutions. Moreover, the present results show more oscillations (small amplitude) than the other solutions.

6.3.2. Exponentially graded materials in the x-direction

Material properties varying along the x-direction are employed to investigate DSIFs for non-homogeneous materials. The material gradation parameter β_1 is chosen as 0.0, 0.05, 0.1 and 0.15, and β_2 is set to zero. The ratio of material properties at the left and right boundaries ranges from 1.0 to 90.0. Although this high material ratio, i.e., 90, is not realistic, such high material gradation is adopted in order to clearly observe the influence of different material profiles on the variation of DSIFs.

Fig. 22 illustrates the variation of mixed mode DSIFs at the left and right crack tip locations. The ordinate indicates normalized DSIFs and the abscissa indicates time up to 20 μs. Both crack tips have the same initiation time for the different material gradations because Young's modulus and mass density follow the same exponential function. As the parameter β_1 increases, the magnitude of $K_I(t)$ at the right crack tip increases. At the left crack tip, up to around 15 μs, the magnitude of $K_I(t)$ is larger for smaller values of β_1 and after that time, the magnitude of $K_I(t)$ becomes smaller for smaller values of β_1. For $K_{II}(t)$, as β_1 increases, the absolute magnitude of $K_{II}(t)$ at both crack tips first decreases and then increases. Moreover, the absolute value of maximum $K_I(t)$ at the right crack tip is higher than that at the left crack tip as β_1 increases. This behavior is reasonable because the material property values at the right crack tip are higher than those at the left crack tip.

6.3.3. Discussion of M-integral terms for non-homogeneous materials

In Section 6.1.6, the contribution of each term was explored thoroughly for homogeneous materials. To account for material non-homogeneity in the current specimen, the M-integral includes Terms 4 and 5. In this section, we examine the influence of each term of the M-integral. Also, we discuss the influence of domain size on the magnitude of Terms 4, 5 and 6, which account for material non-homogeneity and

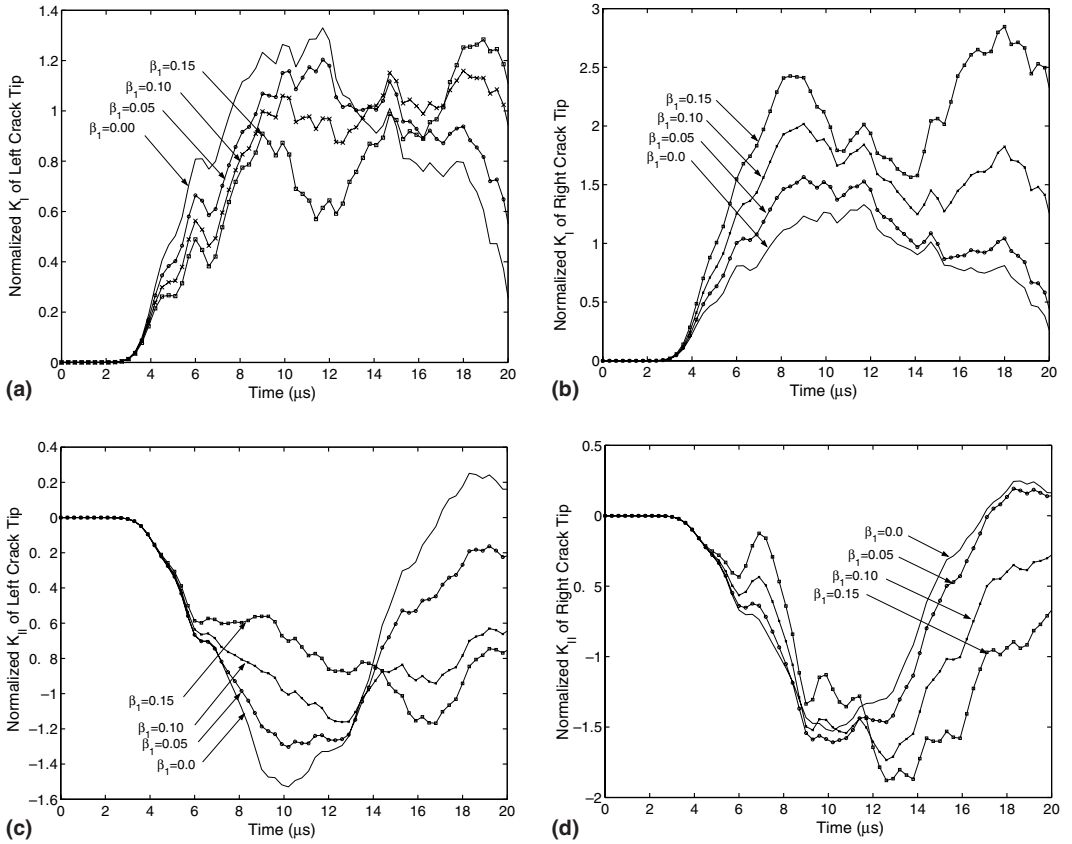

Fig. 22. Mixed mode DSIFs: (a) normalized $K_I(t)$ at the left crack tip; (b) normalized $K_I(t)$ at the right crack tip; (c) normalized $K_{II}(t)$ at the left crack tip; (d) normalized $K_{II}(t)$ at the right crack tip.

dynamic effects. The four different contours illustrated in Fig. 20(c) are used. The value of β_1 is chosen as 0.1 and β_2 is chosen as zero, i.e., $(\beta_1, \beta_2) = (0.1, 0.0)$. The element type, numerical schemes and time step are the same as in the homogeneous case for this specimen.

Fig. 23 shows the contribution of individual terms to normalized DSIFs, $K_I(t)/K_s$ and $K_{II}(t)/K_s$ where K_s is given by Eq. (50), versus time at both the right and left crack-tip locations for the four different contours. The different terms are given by Eqs. (53)–(58). For contour 1, Terms 4 and 5, representing non-homogeneous material effects, and Term 6, accounting for dynamic effects, are small. This shows numerically that the influence of inertia and material non-homogeneity on DSIFs is almost negligible very near the crack tip. Overall, the trend and contribution of Terms 1 and 2 are similar for all contours. During the time period up to 20 μs, Terms 1, 2, 3 and 5 are positive, Term 4 is negative, and Term 6 oscillates. Notice that even though the contribution of each term varies for different contours, the total K is the same for each contour, demonstrating domain independence. We now discuss two important observations: (1) The effects of domain size on non-homogeneous and dynamic terms; (2) the relationship between initiation time and domain size.

Fig. 24(a)–(c), respectively, illustrate the contribution of Terms 4, 5 and 6 for different domain sizes. As we increase the domain size from contour 1 to contour 4, the contribution of Terms 4 and 5, which account for material non-homogeneity, increases and Term 6, which represents dynamic effects, increases in magnitude as well. Therefore, if we neglect these terms in evaluating the M-integral for non-homogeneous

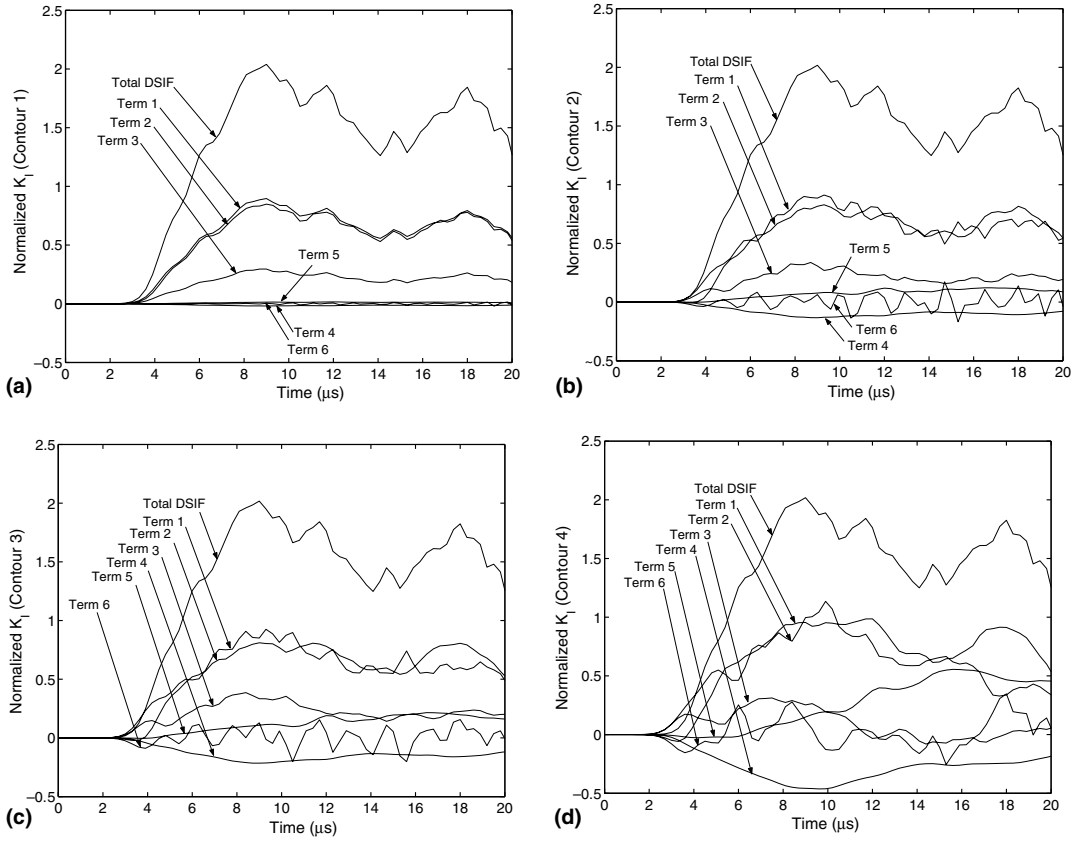

Fig. 23. Contribution of individual terms to the DSIFs for different contours: (a) contribution of each term for contour 1; (b) contribution of each term for contour 2; (c) contribution of each term for contour 3; (d) contribution of each term for contour 4.

cracked specimen under dynamic loadings, domain independence is violated and accuracy worsens as the domain size increases.

Fig. 25(a) and (b) shows the initiation time of each term for contours 1 and 4, respectively. For both figures, the abscissa indicates time from 1.5 μs to 3.5 μs and the ordinate indicates normalized $K_I(t)$. For contour 1, each term and the total DSIF initiate at the same time denoted by T in Fig. 25(a). For contour 4, however, the initiation time of Terms 1, 2, 3 and 6, T_1 in Fig. 25(b), is less than that of total DSIF, i.e., T. It is reasonable because waves reach the boundary of larger domains earlier than the boundary of small domains. On the contrary, initiation time T of Terms 4 and 5 and total DSIF are almost identical. Notice that even though a few terms initiate early, the initiation time of the total DSIF for different contours is the same satisfying domain independence.

6.4. Rectangular plate with cracks emanating from a circular hole

Fedelinski et al. (1994) used the dual BEM and $\widehat{J}$ integral to determine DSIFs in a rectangular plate with cracks emanating from a circular hole. A decomposition procedure was employed for mode mixity. Various angles which range from 0° to 60° were adopted to investigate fracture behavior in terms of the variation of DSIFs. In this study, crack angles of 30° are chosen to investigate the influence of material gradation on DSIFs for non-homogeneous materials.

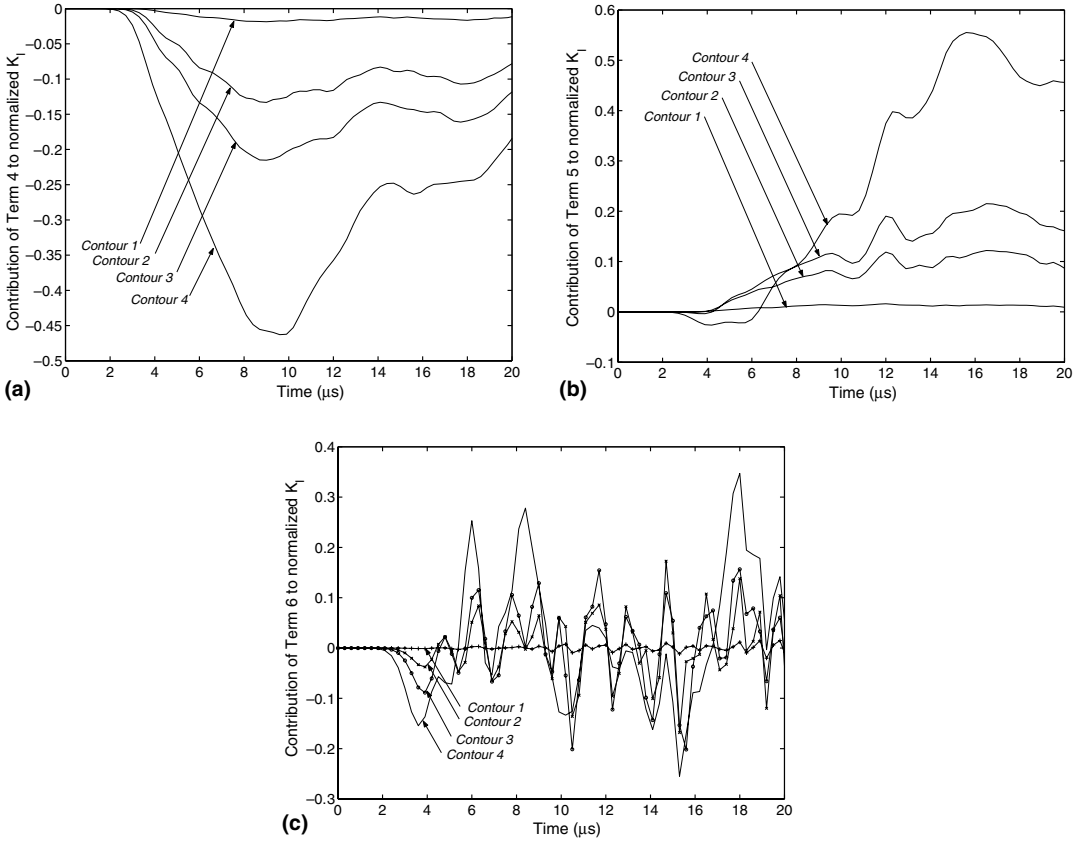

Fig. 24. The influence of domain size on the contribution of each term to DSIFs: (a) Term 4 contribution; (b) Term 5 contribution; (c) Term 6 contribution.

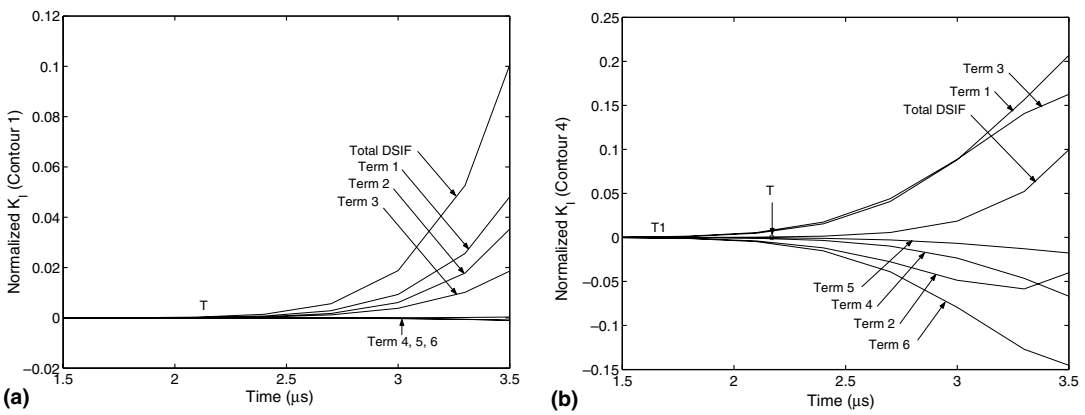

Fig. 25. Relationship between domain size and initiation time of each term in the M-integral: (a) normalized $K_{\mathrm{I}}(t)$ at right crack tip for contour 1; (b) normalized $K_{\mathrm{I}}(t)$ at right crack tip for contour 4.

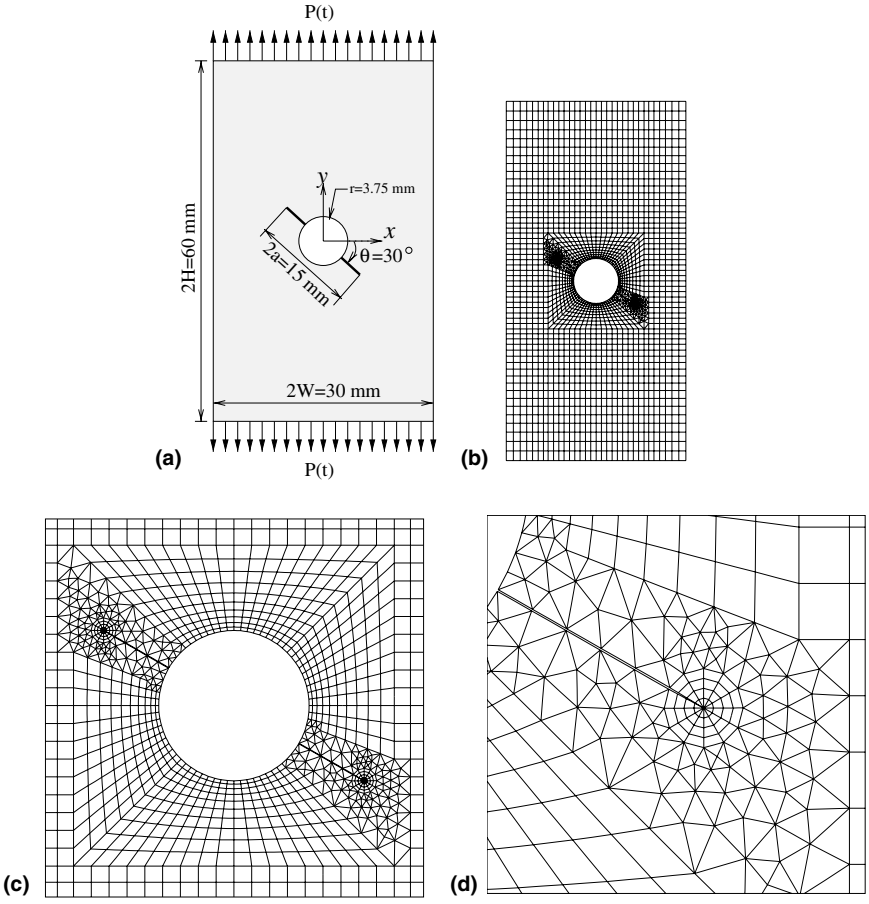

Fig. 26. Rectangular plate with cracks emanating from a circular hole: (a) geometry and boundary conditions; (b) mesh configuration for whole geometry; (c) mesh details for both crack tip regions; (d) mesh details for the right crack tip (12 sectors and 4 rings).

Fig. 26(a) illustrates a rectangular finite plate with a width $2W = 30$ mm and a height $2H = 60$ mm containing a hole of radius $r = 3.75$ mm. Two cracks extend from the hole, and the length between the two crack tips is 15 mm. The cracks are inclined at 30° clockwise from horizontal. Fig. 26(b)–(d) shows the mesh configurations for the whole geometry, and mesh detail for near the hole and the crack tips. A crack tip template of 12 sectors and 4 rings of elements provide sufficient mesh refinement around the crack tip regions, which is crucial to obtain reliable numerical results. Step loading, which is illustrated in Fig. 10, is applied to both the top and bottom edges. In this mesh, 1350 Q8 and 204 T6 plane strain elements are used with 3×3 Gauss quadrature. A time step is $\Delta t = 0.1$ μs.

6.4.1. Homogeneous plate

A comparison between the present numerical results and a reference solution is carried out. For the homogeneous plate, the material properties described in Section 6.3.1 are used. The corresponding wave speeds are given by Eqs. (47)–(49).

Fig. 27 shows the comparison between present numerical results at the right crack tip and the solutions by Fedelinski et al. (1994). The reference results plotted here are obtained from graphical data using

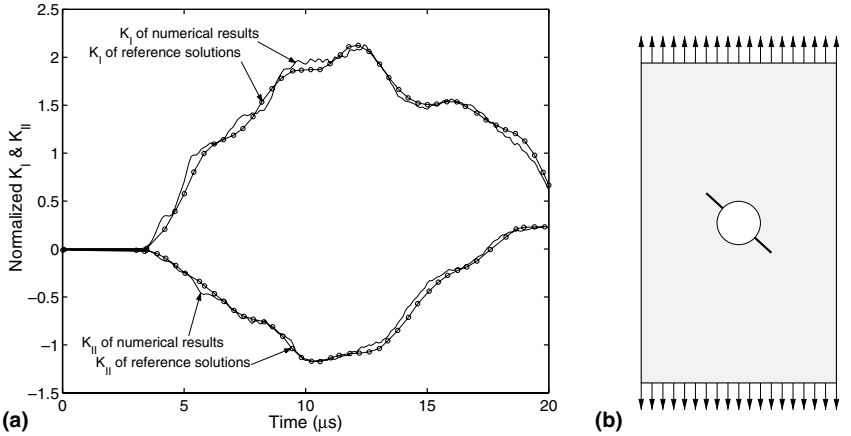

Fig. 27. The comparison between the present numerical results and reference solutions (Fedelinski et al., 1994).

special-purpose software. The abscissa indicates time up to 20 μs. The DSIFs are normalized by K_s given in Eq. (50). The values of $K_{II}(t)$ in Fedelinski et al. (1994) are positive, while the present numerical values of $K_{II}(t)$ are negative up to around 18 μs in Fig. 27. This might be due to different sign convention in shear. The same magnitude but opposite sign of the $K_{II}(t)$ in the reference solution is compared with the present numerical values of $K_{II}(t)$. Greater but acceptable difference is found for $K_I(t)$ values than for $K_{II}(t)$ values.

Table 3
Material properties and dilatational wave speed along the left and right edges

	Young's modulus (MPa)	Mass density (kg/m^3)	Longitudinal wave speed (mm/μs)
Left edge	3811	948	2.33
Right edge	11,130	1812	2.88

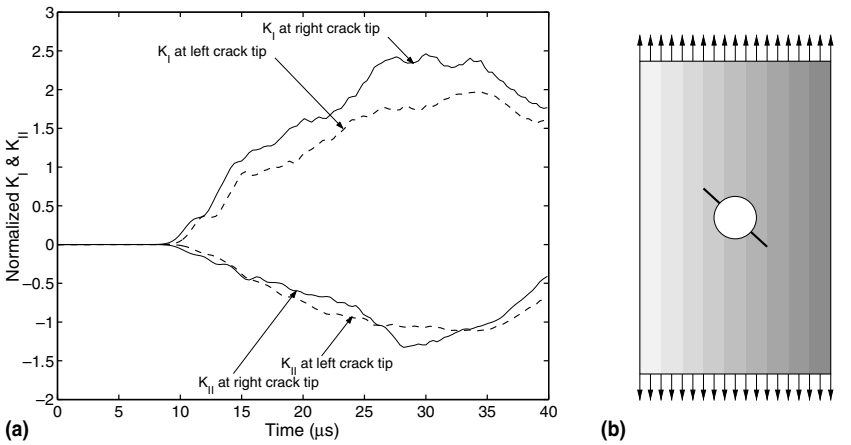

Fig. 28. Normalized mixed-mode DSIFs at both the left and right crack tips for non-homogeneous materials.

The difference may be due to different numerical schemes, different domain discretization, and different conservation integrals; $\widehat{J}$ integral and M-integral. Overall, the present numerical results agree well with this reference solution.

6.4.2. Non-homogeneous plate

In this example, real non-homogeneous material properties prepared by Rousseau and Tippur (2001) are adopted here to investigate fracture behavior. They prepared three point bending specimens made of epoxy and solid soda-lime glass spheres. The material properties of the current specimen possess the values provided in Rousseau and Tippur (2001) and assume linear variation of material properties in the x-direction, which is described by

$$E(x) = (244x + 7471)\ (\text{MPa}), \tag{64}$$

$$\rho(x) = (28.8x + 1380)\ (\text{kg/m}^3). \tag{65}$$

A constant Poisson's ratio of 0.3 is used. Table 3 shows material properties and the corresponding dilatational wave speed along the left edge and the right edge. Notice that the longitudinal wave speed is different at each location due to the different variation between Young's modulus and mass density.

Normalized mixed-mode DSIFs at both the right and left crack tip locations are plotted versus time in Fig. 28. The ordinate indicates DSIFs normalized by K_s (see Eq. (50)) and the abscissa is time up to 40 μs. Since initiation time of DSIFs depends on the dilatational wave speed, first the DSIFs at the right crack tip initiate, and then, the DSIFs at the left crack tip initiate as shown in Fig. 28. At any given time of the transient response, the magnitude of $K_I(t)$ at the right crack tip is higher than that at the left crack tip for the non-homogeneous case. This is due to the fact that the values of material properties at the right crack tip are higher than those at the left crack tip.

7. Conclusion

Dynamic fracture behavior for both homogeneous and non-homogeneous materials is examined thoroughly in this study. The M-integral is superior to the DCT in terms of accuracy, and unlike the standard J-integral, it yields mixed-mode SIFs directly. Thus, the M-integral is extended to incorporate the material non-homogeneity and dynamic effects. Notice that Williams' solution (1957) is employed as dynamic auxiliary fields because the asymptotic singular stress fields in non-homogeneous materials under dynamic condition are shown to have similar behaviors with those in homogeneous materials under quasi-static condition (Eischen, 1987; Freund, 1998; Freund and Clifton, 1974; Nilsson, 1974; Parameswaran and Shukla, 1999). The non-equilibrium formulation of the M-integral is employed here to evaluate SIFs for both static and dynamic cases. The research code, which has been developed using the implicit time scheme and the M-integral with graded elements by means of the GIF (Kim and Paulino, 2002a), is verified using benchmark problems. Using the verified code, fracture problems are presented and discussed. In non-homogeneous media, variation of DSIFs is hard to be generalized because it is highly dependent upon geometry, material gradation and boundary conditions. However, as seen in the previous examples, e.g., Fig. 22, the magnitude of DSIFs at the crack tip located in the stiffer part increases overall, as material gradation increases, i.e., β increases.

The major contributions of this study can be summarized as follows:

- The M-integral based on the non-equilibrium formulation is derived to account for material non-homogeneity and dynamic effects.
- The mode I and mixed mode DSIFs for both homogeneous and non-homogeneous materials are evaluated using the M-integral.

- The domain independence of the M-integral is assessed numerically for both homogeneous and non-homogeneous materials under dynamic loading.
- Fracture behavior is investigated thoroughly for homogeneous and non-homogeneous materials under dynamic loading, including the influence of material gradation on variations of DSIFs, the relation between initiation time and the domain size, and the contribution of each distinct term in the M-integral.

Acknowledgement

We are grateful to the support from the National Science Foundation (NSF) through the GOALI project CMS 0219566 (Program Manager, P. N. Balaguru). Any opinions expressed herein are those of the writers and do not necessarily reflect the views of the sponsors.

Appendix A. Numerical implementation details

The displacement field of Williams' (1957) solution can be rewritten as

$$u^{\ell}(r,\theta)_i^{\text{aux}} = \frac{K_{\text{I}}^{\text{aux}}}{\mu_{\text{tip}}} g_i^{\text{I}}(r,\theta) + \frac{K_{\text{II}}^{\text{aux}}}{\mu_{\text{tip}}} g_i^{\text{II}}(r,\theta) \quad (i=1,2), \tag{66}$$

where superscript ℓ means local coordinate. The derivatives of auxiliary displacements with respect to the global coordinate systems are calculated as follows ($k=1,2$):

$$u^{\text{g}}(r,\theta)_{i,k}^{\text{aux}} = \frac{\partial u^{\text{g}}(r,\theta)_i^{\text{aux}}}{\partial X_k} = \frac{\partial u^{\text{g}}(r,\theta)_i^{\text{aux}}}{\partial r}\frac{\partial r}{\partial X_k} + \frac{\partial u^{\text{g}}(r,\theta)_i^{\text{aux}}}{\partial \theta}\frac{\partial \theta}{\partial X_k}, \tag{67}$$

where

$$\begin{Bmatrix} u^{\text{g}}(r,\theta)_1^{\text{aux}} \\ u^{\text{g}}(r,\theta)_2^{\text{aux}} \end{Bmatrix} = \begin{bmatrix} \cos\alpha & -\sin\alpha \\ \sin\alpha & \cos\alpha \end{bmatrix} \begin{Bmatrix} u^{\ell}(r,\theta)_1^{\text{aux}} \\ u^{\ell}(r,\theta)_2^{\text{aux}} \end{Bmatrix} \tag{68}$$

and

$$\frac{\partial r}{\partial X_k} = \frac{\partial r}{\partial x_1}\frac{\partial x_1}{\partial X_k} + \frac{\partial r}{\partial x_2}\frac{\partial x_2}{\partial X_k}, \quad \frac{\partial \theta}{\partial X_k} = \frac{\partial \theta}{\partial x_1}\frac{\partial x_1}{\partial X_k} + \frac{\partial \theta}{\partial x_2}\frac{\partial x_2}{\partial X_k}, \tag{69}$$

with

$$\begin{aligned} &\partial r/\partial x_1 = \cos\theta, \quad \partial r/\partial x_2 = \sin\theta, \\ &\partial\theta/\partial x_1 = -\sin\theta/r, \quad \partial\theta/\partial x_2 = \cos\theta/r, \\ &\partial x_1/\partial X_1 = \cos\alpha, \quad \partial x_1/\partial X_2 = \sin\alpha, \\ &\partial x_2/\partial X_1 = -\sin\alpha, \quad \partial x_2/\partial X_2 = \cos\alpha. \end{aligned} \tag{70}$$

As illustrated in Fig. 4, α is the angle between global and local coordinates, r is the radial distance, and θ is the angle between local and the point where field quantities are obtained. Notice that (x_1, x_2) and (X_1, X_2) indicate local and global coordinates, respectively.

Due to the non-equilibrium formulation, the auxiliary strain field is obtained using the compatibility condition as

$$\varepsilon^{\text{g}}(r,\theta)_{ij}^{\text{aux}} = \frac{1}{2}\left(u^{\text{g}}(r,\theta)_{i,j}^{\text{aux}} + u^{\text{g}}(r,\theta)_{j,i}^{\text{aux}}\right), \tag{71}$$

where $u^{g}(r,\theta)_{i,j}$ is obtained using Eq. (66).

The auxiliary stress is evaluated using the constitutive relationship

$$\sigma^{g}(r,\theta)^{aux}_{ij} = C_{ijkl}(\boldsymbol{x})\varepsilon^{g}(r,\theta)^{aux}_{kl}. \tag{72}$$

The material properties used in the constitutive tensor are computed using the isoparametric formulation (Kim and Paulino, 2002a).

The derivative of the auxiliary stress is given by

$$(\sigma^{g}(r,\theta)^{aux}_{ij})_{,j} = (C_{ijkl}(\boldsymbol{x})\varepsilon^{g}(r,\theta)^{aux}_{kl})_{,j} = C_{ijkl,j}\varepsilon^{g}(r,\theta)^{aux}_{kl} + C_{ijkl}\varepsilon^{g}(r,\theta)^{aux}_{kl,j}, \tag{73}$$

where the derivative of auxiliary fields with respect to global coordinates, $\varepsilon^{g}(r,\theta)^{aux}_{kl,j}$, is evaluated as follows:

$$\varepsilon^{g}(r,\theta)^{aux}_{ij,k} = \frac{\partial\varepsilon^{g}(r,\theta)^{aux}_{ij}}{\partial X_k} = \frac{\partial\varepsilon^{g}(r,\theta)^{aux}_{ij}}{\partial r}\frac{\partial r}{\partial X_k} + \frac{\partial\varepsilon^{g}(r,\theta)^{aux}_{ij}}{\partial\theta}\frac{\partial\theta}{\partial X_k}. \tag{74}$$

In computing Eq. (74), the Eqs. (69) and (70) are used.

References

ABAQUS, 2004. Version 6.4, H.K.S. Inc., Pawtucket, RI.

Anderson, T.L., 1995. Fracture Mechanics: Fundamentals and Application. CRC, Boca Raton.

Aoki, S., Kishimoto, K., Kondo, H., Sakata, M., 1978. Elastodynamic analysis of crack by finite element method using singular element. International Journal of Fracture 14 (1), 59–67.

Belytschko, T., Lu, Y.Y., Gu, L., Tabbara, M., 1995. Element free Galerkin methods for static and dynamic fracture. International Journal of Solids and Structures 32 (17/18), 2547–2570.

Brickstad, B., 1983. A FEM analysis of crack arrest experiments. International Journal of Fracture 21 (3), 177–194.

Bui, H.D., 1983. Associated path independent *J*-integrals for separating mixed modes. Journal of the Mechanics and Physics of Solids 31 (6), 439–448.

Buttlar, W.G., Paulino, G.H., Song, S.H., 2005. Application of graded finite elements for asphalt pavement analysis. ASCE Journal of Engineering Mechanics, in press.

Chen, Y.M., 1975. Numerical computation of dynamic stress intensity factors by a Lagrangian finite-difference method (the HEMP code). Engineering Fracture Mechanics 7 (4), 653–660.

Chen, Y.M., Wilkins, M.L., 1976. Stress analysis of crack problems with a three dimensional time dependent computer program. International Journal of Fracture 12 (4), 607–617.

Dolbow, J., Gosz, M., 2000. On the computation of mixed-mode stress intensity factors in functionally graded materials. International Journal of Solids and Structures 39 (9), 2557–2574.

Dominguez, J., Gallego, R., 1992. Time domain boundary element method for dynamic stress intensity factor computations. International Journal for Numerical Methods in Engineering 33 (3), 635–647.

Eftis, J., Subramonian, N., Liebowitz, H., 1977. Crack border stress and displacement equation revisited. Engineering Fracture Mechanics 9 (1), 189–210.

Eischen, J.W., 1987. Fracture of non-homogeneous materials. International Journal of Fracture 34 (1), 3–22.

Enderlein, M., Ricoeur, A., Kuna, M., 2003. Comparison of finite element technique for 2D and 3D crack analysis under impact loading. International Journal of Solids and Structures 40 (13–14), 3425–3437.

Fedelinski, P., 2004. Boundary element method in dynamic analysis of structures with cracks. Engineering Analysis with Boundary Elements 28 (9), 1135–1147.

Fedelinski, P., Aliabadi, M.H., Rooke, D.P., 1994. The dual boundary element method: $\widehat{J}$-integral for dynamic stress intensity factors. International Journal of Fracture 65 (4), 369–381.

Freund, L.B., 1998. Dynamic Fracture Mechanics. Cambridge University Press, Cambridge.

Freund, L.B., Clifton, R.J., 1974. On the uniqueness of plane elastodynamic solutions for running cracks. Journal of Elasticity 4 (4), 293–299.

Fung, Y.C., 1965. Foundation of Solid Mechanics. Prentice-Hall, Englewood Cliffs, NJ.

Hughes, T.J.R., 1987. The Finite Element Method: Linear Static and Dynamic Finite Element Analysis. Prentice-Hall, New Jersey.
Kim, J.-H., Paulino, G.H., 2002a. Isoparametric graded finite elements for non-homogeneous isotropic and orthotropic materials. ASME Journal of Applied Mechanics 69 (4), 502–514.
Kim, J.-H., Paulino, G.H., 2002b. Finite element evaluation of mixed mode stress intensity factors in functionally graded materials. International Journal for Numerical Methods in Engineering 53 (8), 1903–1935.
Kim, J.-H., Paulino, G.H., 2003a. T-stress, mixed-mode stress intensity factors, and crack initiation angles in functionally graded materials: a unified approach using the interaction integral method. Computer Methods in Applied Mechanics and Engineering 192 (11/12), 1463–1494.
Kim, J.-H., Paulino, G.H., 2003b. An accurate scheme for mixed-mode fracture analysis of functionally graded materials using the interaction integral and micromechanics models. International Journal for Numerical Methods in Engineering 58 (10), 1457–1497.
Kim, J.-H., Paulino, G.H., 2005. Consistent formulations of the interaction integral method for fracture of functionally graded materials. ASME Journal of Applied Mechanics 72 (3), 351–364.
Kishimoto, K., Aoki, S., Sakata, M., 1980. Dynamic stress intensity factors using *J*-integral and finite element method. Engineering Fracture Mechanics 13 (2), 387–394.
Konda, N., Erdogan, F., 1994. The mixed mode crack problem in a non-homogeneous elastic medium. Engineering Fracture Mechanics 47 (4), 533–545.
Krysl, P., Belytschko, T., 1999. The element free Galerkin method for dynamic propagation of arbitrary 3-D cracks. International Journal for Numerical Methods in Engineering 44 (6), 767–800.
Lee, Y.J., Freund, L.B., 1990. Fracture initiation due to asymmetric impact loading of an edge cracked plate. ASME Journal of Applied Mechanics 57 (1), 104–111.
Lin, X., Ballmann, J., 1993. Re-consideration of Chen's problem by finite difference method. Engineering Fracture Mechanics 44 (5), 735–739.
Moran, B., Shih, F.C., 1987. Crack tip and associated domain integrals from momentum and energy balance. Engineering Fracture Mechanics 27 (6), 615–642.
Murti, V., Valliappan, S., 1986. The use of quarter point element in dynamic crack analysis. Engineering Fracture Mechanics 23 (3), 585–614.
Newmark, N.M., 1959. A method of computation for structural dynamics. ASCE Journal of Engineering Mechanics 85 (EM3, Part 1), 67–94.
Nilsson, F., 1974. A note on the stress singularity at a non-uniformly moving crack tip. Journal of Elasticity 4 (1), 73–75.
Parameswaran, V., Shukla, A., 1999. Crack tip stress fields for dynamic fracture in functionally gradient materials. Mechanics of Materials 31 (9), 579–596.
Raju, I.S., Shivakumar, K.N., 1990. An equivalent domain integral method in the two dimensional analysis of mixed mode crack problems. Engineering Fracture Mechanics 37 (4), 707–725.
Rao, B.N., Rahman, S., 2003. Mesh-free analysis of cracks in isotropic functionally graded materials. Engineering Fracture Mechanics 70 (1), 1–27.
Rice, J.R., 1968. A path-independent integral and the approximate analysis of strain concentration by notches and cracks. ASME Journal of Applied Mechanics 35 (2), 379–386.
Rousseau, C.-E., Tippur, H.V., 2001. Dynamic fracture of compositionally graded materials with cracks along the elastic gradient: experiment and analysis. Mechanics of Materials 33 (7), 403–421.
Santare, M.H., Lambros, J., 2000. Use of graded finite elements to model the behavior of non-homogeneous materials. Journal of Applied Mechanics—Transactions ASME 67 (4), 819–822.
Santare, M.H., Thamburaj, P., Gazonas, G.A., 2003. The use of graded finite elements in the study of elastic wave propagation in continuously non-homogeneous materials. International Journal of Solids and Structures 40 (21), 5621–5634.
Shih, C.F., deLorenzi, H.G., German, M.D., 1976. Crack extension modeling with singular quadratic isoparametric elements. International Journal of Fracture 12 (4), 647–651.
Sladek, J., Sladek, V., Fedelinski, P., 1997. Integral formulation for elastodynamic T-stresses. International Journal of Fracture 84 (2), 103–116.
Sladek, J., Sladek, V., Fedelinski, P., 1999. Computation of the second fracture parameter in elastodyanamics by the boundary element method. Advances in Engineering Software 30 (9/11), 725–734.
Song, S.H., 2003. Dynamic stress intensity factors for homogeneous and non-homogeneous materials using the interaction integral method, Master Thesis, Department of Civil and Environmental Engineering, University of Illinois at Urbana-Champaign.
Tabiei, A., Wu, J., 2003. Development of the DYNA3D simulation code with automated fracture procedure for brick elements. International Journal for Numerical Methods in Engineering 57 (14), 1979–2006.
Whirley, R.G., Engelmann, B.E., 1993. DYNA3D User Manual, Lawrence Livermore National Laboratory.
Williams, M.L., 1957. On the stress distribution at the base of a stationary crack. ASME Journal of Applied Mechanics 24 (1), 109–114.

Wu, C.-C., He, P., Li, Z., 2002. Extension of *J* integral to dynamic fracture of functional graded material and numerical analysis. Computers and Structures 80 (5/6), 411–416.

Yau, J.F., Wang, S.S., Corten, H.T., 1980. A mixed mode crack analysis of isotropic solids using conservation laws of elasticity. ASME Journal of Applied Mechancis 47 (2), 335–341.

Zhang, Ch., 2002. A 2D hypersingular time domain traction BEM for transient elastodynamic crack analysis. Wave Motion 35 (1), 17–40.